Kaunas University of Technology

Faculty of Mathematics and Natural Sciences

Dosimetry Measurements with Anthropomorphic Phantom SHANE Imitating Irradiation for Head and Neck Cancer Patient

Master's Final Degree Project

Koshal Bhatta

Project author

Assoc. Prof. dr. Jurgita Laurikaitienė

Supervisor

Kaunas, 2021

Kaunas University of Technology

Faculty of Mathematics and Natural Sciences

Dosimetry Measurements with Anthropomorphic Phantom SHANE Imitating Irradiation for Head and Neck Cancer Patient

Master's Final Degree Project

Medical Physics (6213GX001)

Koshal Bhatta

Project author

Assoc. Prof. dr. Jurgita Laurikaitienė

Supervisor

Aleksandras ILJINAS

Reviewer.

Kaunas, 2021

Kaunas University of Technology

Faculty of Mathematics and Natural sciences

Koshal Bhatta

Dosimetry Measurements with Anthropomorphic Phantom SHANE Imitating Irradiation for Head and Neck Cancer Patient

Declaration of Academic Integrity

I confirm that the final project of mine, Koshal Bhatta, on the topic "Dosimetry Measurements with Anthropomorphic Phantom SHANE Imitating Irradiation for Head and Neck Cancer Patient" is written completely by myself; all the provided data and research results are correct and have been obtained honestly. None of the parts of this thesis have been plagiarised from any printed, Internet-based or otherwise recorded sources. All direct and indirect quotations from external resources are indicated in the list of references. No monetary funds (unless required by Law) have been paid to anyone for any contribution to this project.

I fully and completely understand that any discovery of any manifestations/case/facts of dishonesty inevitably results in me incurring a penalty according to the procedure(s) effective at Kaunas University of Technology.

Koshal Bhatta

(name and surname filled in by hand) (signature)

Koshal Bhatta. Dosimetry accuracy for head and neck irradiation simulation using SHANE phantom. Research project/Supervisor Assoc. Prof. Dr Jurgita Laurikaitaitiene; Faculty of Mathematics and Natural science, Kaunas University of technology.

Study field and area (Study field group): Health Sciences, Medical Technologies (G09).

Keywords: VMAT, SHANE phantom, Quality control, OCTAVIUS 729 Detector.

Kaunas, 2021, 66 Pages.

Summary

Dosimetric measurement is a vital component for clinical procedures, especially for Intensity-Modulated Radiotherapy and Volumetric Modulated Arc radiotherapy. These procedures require the use of tailored phantoms for quality assurance, which has a variety of shortcomings such as homogenous materials unable to mimic the true radiation attenuation properties of the human body. The SHANE phantom is introduced to tackle these shortcomings and the purpose of this thesis is to perform an accurate dosimetric evaluation with phantom SHANE for head and neck cancer.

The experiment was performed using two medical linear accelerators Elekta infinity (Monaco TPS) and Varian Halcyon (Eclipse TPS) at Siauliai Hospital department of radiotherapy and Onkologinė ligoninė, Volungių g. 16, Kaunas respectively with photon energy 6 MeV (max). The ion chamber, electrometer, and SHANE phantom are the main equipment used. Different MLC field size tests, in-plane, and cross-plane profile tests were performed in the treatment planning system using virtual water phantom. The treatment planning system was done for VMAT delivery technique with simultaneous integrated boost (SIB) using Monaco treatment planning system (TPS) for linear accelerator (LA) Electra infinity and LA Eclipse for Halcyon. Three PTV (PTV_7000, PTV_6000, and PTV_5400) was assigned the dose 70 Gy, 60 Gy, and 54 Gy respectively with 30 fraction and spinal cord as organ at risk. The patient-specific quality assurance was performed using the Octavius detector.

The dose difference for ion chamber measurement and treatment planning calculated dose using Eclipse TPS for (all four points of measurement IC_PTV_7000 (1.13 %), IC_PTV_6000(1.34 %), IC_ PTV_5400 (1.06 %), and for IC_spinal cord (2.95 %) are within the tolerance limit of 5% for PTVs and 7% the organ at risk spinal cord. Similar tendency was observed for the LA *Halcyon*: IC_PTV_7000 (12.85 %), IC_PTV_6000 (1.60 %) and IC_ PTV_5400 (3.05 %) and for IC_spinal cord (2.57 %) are within the tolerance limit of 5 %-7%, except IC PTV 7000.

Koshalas Bhatta. Dozimetrijos tikslumas galvos ir kaklo švitinimo modeliavimui naudojant SHANE fantomą. Tyrimo projektas / Vadovas doc. Prof. Dr. Jurgita Laurikaitaitienė; Kauno technologijos universiteto Matematikos ir gamtos mokslų fakultetas.

Studijų sritis ir sritis (Studijų krypties grupė): Sveikatos mokslai, Medicinos technologijos (G09).

Raktiniai žodžiai: VMAT, SHANE fantomas, kokybės kontrolė, OCTAVIUS 729 detektorius.

Kaunas, 2021, 66 psl.

Summary

Dozimetrinis matavimas yra gyvybiškai svarbus komponentas atliekant klinikines procedūras, ypač atliekant intensyvumo moduliuojamą radioterapiją ir tūrinę moduliuojamo lanko radioterapiją. Šioms procedūroms užtikrinti kokybę reikia naudoti specialiai pritaikytus fantomus, kurie turi įvairių trūkumų, tokių kaip homogeniškos medžiagos, negalinčios imituoti tikrųjų žmogaus kūno radiacijos slopinimo savybių. SHANE fantomas yra pristatytas siekiant pašalinti šiuos trūkumus, o šios baigiamojo darbo tikslas yra tiksliai ir tiksliai įvertinti galvos ir kaklo vėžio dozimetrinį įvertinimą SHANE.

Eksperimentas buvo atliktas naudojant du medicininius linijinius greitintuvus (LG) „Electa Infinity“ (spindulinio gydymo planavimo sistema (SGPS) „Monaco“) ir LG „Halcyon“ (SGPS „Eclipse“) Šiaulių Respublikinės ligoninės radioterapijos skyriuje ir Lietuvos sveikatos mokslų universiteto ligoninės Kauno klinikų filiale, Onkologijos ligoninėje, Spindulinio gydymo sektoriuje, atitinkamai su didelės energijos fotonais (6 MeV). Jonizacinė kamera, elektrometras ir antropomorfinis fantomas SHANE, tai pagrindinės priemonės naudojamos dozimetriniams matavimams atlikti. Skirtingo lauko dydžio testas buvo atliktas naudojant virtualų vandens fantomą. Antropomorfinis fantomas „Shane“ buvo nuskenuotas kompiuteriniu tomografu „Philips Brilliance Big Bore“. Gydymo planavimas buvo atliktas naudojant tūrinės moduliuotos arkinės terapijos metodiką, naudojant spindulinio gydymo planavimo sistemą „Monaco“ linijiniam greitintuvui (LG) „Electa Infinity“ ir SGPS „Eclipse“ LG „Halcyon“. Trims planuojamiems taikinio tūriams (PTV_7000, PTV_6000 ir PTV_5400) su atitinkamomis apšvitos dozėmis 70 Gy, 60 Gy ir 54 Gy (iš viso 30 frakcijų), vertinant nugaros smegenis kaip kritinė organą. Kokybės užtikrinimas buvo atliktas naudojant „Octavius“ detektorių.

Apšvitos dozių vertinimas, remiantis spindulinio gydymo planavimo sistemos „Monaco“ skaičiavimo rezultatais (keturi matavimo taškai IC_PTV_7000 (1,13%), IC_PTV_6000 (1,34%) ir IC_ PTV_5400 (1,06%) bei nugaros smegenys (2,95%)) neviršija 5% planuojamiems taikinio tūriams ir 7% kritiniam organui (nugaros smegenims) tolerancijos ribos. Panaši tendencija pastebėta ir LG „Halcyon“: IC_PTV_7000 (12,85%), IC_PTV_6000 (1,60%) ir IC_ PTV_5400 (3,05%) ir nugaros smegenims (2,57%) neviršija 5% -7% tolerancijos ribos, išskyrus IC PTV 7000. Planuojamiems taikinių tūriams homogeniškumo indeksas parodo geresnį taikinio apsiėmimą.

Acknowledgement

I would like to express my deeper appreciation to my research supervisor Assoc. prof. Dr Jurgita Laurikaitienė, Kaunas University of Technology, and also far medical physicist Karolis Jakštas and Genadij Aleksejenko, Šiauliai Hospital Department of radiotherapy, proving me all the methodological guidance and valuable information through video chat. They provide me the experimental data and taught me to carry out the research. It was a great privilege and honor to work and study under their guidance.

In addition, I would like to thank my family and friends who motivated me to complete my research work on time.

Table of contents

List of figures

List of tables

List of abbreviations

AHRT - Accelerated Hyper fractionated Radiotherapy;

CT – computed tomography;

CBCT - cone-beam computed tomography;

TLD – thermoluminescent dosimeters;

IAEA – International Atomic Energy Agency;

LINAC- linear accelerator;

3D-CRT - three-dimensional conformal radiation therapy;

IMRT -intensity-modulated radiation therapy;

VMAT- Volumetric modulated arch radiotherapy;

MLC -multileaf collimator;

IGRT- image-guided radiation therapy;

MRI – magnetic resonance imaging;

WHO – World Health Organization;

ICRU – International Commission Radiation Unit;

IC- Ionization chamber;

EPID – electronic portal imaging detector;

MOSFET – metal-oxide semiconductor field effect transistor;

ICRP -International Commission on Radiological Protection;

PMMA -Poly (methyl methacrylate);

PTV- planning target volume;

CTV- clinical target volume;

SIB- simultaneous integrated boost;

3D CRT- three-dimensional conformal radiotherapy;

SBRS- stereotactic body radiosurgery;

MLC- Multi-leaf collimator;

HNSCC- Head and neck squamous cell carcinoma;

LA- linear accelerator;

Introduction

Radiotherapy becomes an effective therapeutic tool to treat cancer for the last 100 years [1]. In advanced radiotherapy, techniques such as intensity-modulated radiotherapy and Volumetric modulated arch radiotherapy deliver a high conformal dose with non-uniform radiation fluence beam towards the patient with the relatively small field up to a few millimetres. The dosimetry for small filed megavoltage photon beam used in IMRT, VMAT, and SBRS required more complex dosimetry protocols and are concerned with the loss of lateral electronic equilibrium, detector size larger than beam dimension and cause the overlap of beam penumbra and detector volume [2]. To validate the desired dose distribution the patient-specific quality assurance is a relevant and important step, which can be performed using different ionization chamber, film, or two-dimensional array matrix.

Commercially available Head and neck phantoms are constrained due to the high production cost and are not appropriate for end-to-end testing in radiotherapy, are constructed based upon the specific patient pathology feature with homogeneous materials which does not adhere to the radiation interaction properties of the human body.

These problems were addressed by using a small-volume ionization chamber for small field size [2, 3] and the new dosimetry audit package introduced by the International Atomic Energy Agency (IAEA) for the overall radiotherapy process using anthropomorphic phantom, which mimics the complex anatomy of the head and neck region [4]. Anthropomorphic phantom becomes a more convenient tool for dosimetry verification as a part of patient-specific quality assurance. The application of an anthropomorphic phantom for dosimetry measurement is associated with the reduction in uncertainty by performing the end-to-end test as for part of comprehensive quality assurance compared to commercially available phantom and now these phantoms are used for the dosimetry audit, which can address the local problem and solve the uncertainty, associated with radiotherapy process.

The research work aims to perform dosimetry measurements using anthropomorphic head and neck phantom SHANE following the main dosimetry audit protocol of end-to-end test.

The tasks:

1. To perform a quality control test for the small fields (2×2) cm^2.
2. To use electron density curve, evaluating possible Hounsfield values deviation.
3. To perform patient-specific quality control test using Octavius detector, evaluating measured gamma factor (3%/3mm).
4. To measure the absorbed dose in four different predefined positions within anthropomorphic phantom SHANE, following the main dosimetry audit protocol of end-to-end test and compare it for two different manufacturer's linear accelerators (Elekta Infinity and Varian Halcyon).

1. Literature review

1.1. Head and Neck cancer

Head and neck (H&N) cancer are reported as the sixth most common cancer around the world with a reported 3% of all cancer with 330,000 deaths among the 650,000 cases [5]. The most common localisations include the pharynx, larynx, paranasal sinus, nasal cavity, oral cavity, and salivary glands of the head and neck. Cancers [5, 6]. Squamous cell carcinoma is the most common cause found in these anatomical structures and is diagnosed when clinical symptoms arise. The most common causes are the consumption of tobacco delivered carcinogens and alcohol along with environmental factors [5]. Tumours developed at the oropharynx are associated with the oncogenetic strain of human papillomavirus (HPV), primarily HPV-16, and to a lesser extent, HPV-18 and other strains and for the oral cavity and larynx are caused by smoking and collectively regarded as HPV-negative H&N Squamous cell carcinoma (HNSCC) [7].

The treatment of head and neck cancer involves chemotherapy, radiation therapy (RT), immunotherapy, or a combination of two different types [5, 8]. Radiotherapy is one of the most commonly used treatment modalities to treat cancer. Radiotherapy involves ionizing radiation to damage the tumour cell by damaging the DNA sequences with minimum exposure to the normal tissue. Intensity-modulated radiotherapy (IMRT) and volumetric modulated arc radiotherapy (VMAT) are the standard irradiation technique used for the HNSCC where the highly conformal dose can be delivered within the tumour volume with minimum exposure to the critical structure [9].

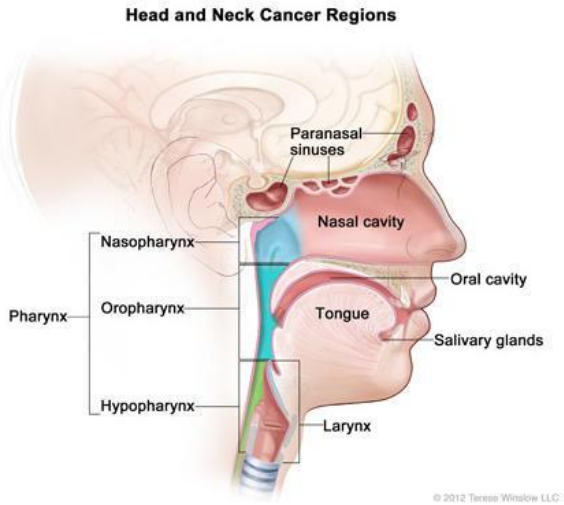

Fig.1. Head and Neck cancer regions [10]

The complex heterogeneous anatomical structure of the H&N region and closed proximity of the critical organ towards the planning tumour volume (PTV) leads to the complex dosimetry protocol for the verification of treatment planning. The irradiation dose value depends on the type, size, location of the tumour, and more importantly the distance from the critical structure. The main organs at risk (OARs) are divided into different categories; optic structure (corona, retina, lens),

salivation-related structure (parotid glands, Submandibular gland, Sublingual gland, Extended oral cavity), structure related to swallowing, brachial plexus, and intracranial structures. These structures are the limiting factor for the dose to the tumour volume [11].

Radio biologically; the outcome of radiotherapy depends on the radiosensitivity of the target and nearby critical structure. For the head and neck region, various radiosensitive organs, for example, thyroid glands, lead to treatment failure if radiation dose exceeds the tolerance level and is a serious problem related to cellular damage. If the absorbed dose is exceeding 30 Gy, it significantly contributed to the risk of hyperthyroidism. Some studies show that thyroid-stimulating hormone also increases when the total dose exceeds 10 Gy during the treatment session. These factors significantly affect the outcome of the radiotherapy treatment. In recent years, radiation sensitization was suggested to solve the challenges of radioresistance by enhancing the radiation damage of the tumour. Each patient, who receives the same fraction of radiation dose, shows a different tumour response due to the complexity and heterogeneity of the tumour [8].

1.2. Radiation therapy

After the discovery of X-ray in 1985 by W.C. Roentgen and A. Becquerel radioactivity (1896) meant the development of radiotherapy. Later on, In 1898 Maria Sklodowska-Curie and Pierre Curie discovered radium and polonium, which can be applied for the high-dose radiation in brachytherapy. A teletherapy unit with a Co-60 source as a gamma-emitter has introduced around the 1950s to 1980s where a Co-60 source is placed in a teletherapy unit head and is used for the treatment of tumours located deeper from the surface.Cobalt-60 units are replaced by the linear accelerator where the particles can accelerate linearly and generate high energetic photons without using a radioactive source [12, 13].

Radiation can be delivered either distinct source called external beam radiotherapy (EBRT), in which a high precise dose can be delivered to cancer cell with minimizing dose to the surrounding structure, or brachytherapy where a radioactive source is injected towards the tumour or near to the tumour and systematic therapy with radioisotope [12]. The main aim of radiotherapy is to destroy the cancer cell with a high radiation dose along with the minimum exposure to the normal tissue. Therefore, the limiting factor for the irradiation dose to the target is the proximity of normal tissue and the radiosensitive normal cells [14]. In (EBRT) radiations; electron beam, photon, neutrons, and particle radiation such as; (proton and heavy) ion beam are used to treat the cancer cells in different regions [15]. Interaction of these radiations to the tumour shows the different radiation damage and depending upon the radiation quality and quantities so that their application varies. The depth dose distribution of different radiation in water is shown in figure (16).

EBRT is applicable for the treatment of various tumour types such as Head and Neck, breast cancer, lungs, prostate, etc. The most applicable brachytherapy source are iodine- 125, gold-198, and iridium-192 are directly inserted toward the tumour. Systematic therapy where radioisotopes such as; iodine- 131, Yttrium-90, Lutetium-177) are used based on their chemical properties [12].

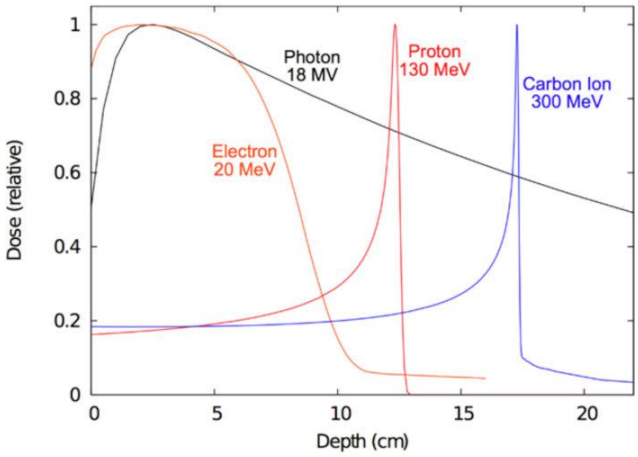

Fig.2. Depth dose distribution for different radiation [16]

The electron beam with the small build-up region, after a certain depth, dose decreases sharply (figure 2) so that, it deposits the maximum energy to the surface so that it is used for the treatment of superficial lesions. The depth dose profile of the photon beam shows the relatively larger build-up region and its interaction shows the exponential attenuation of dose after a certain depth and causes exposure to normal tissue behind the target. In contrast, for the particle radiation; proton and carbon ion at 130 MeV and 300 MeV respectively shows the dapper depth dose distribution with minimal to the entrance surface dose and almost certainty of dose to the target with negligible dose behind the target [16]. These physical nature of proton interaction in a graph called 'Bragg peaks' so that its clinical application increases for the treatment of tumours especially for the head and neck regions with protecting the organ at risks (OARs) with better tissue spearing and have significantly improved the tumour control probability and less toxicity associated with better quality of life [16].

The effect of ionization radiation on tissue is described by various means. The main target of radiation is to damage the tumour cell by halting their repair. The DNA damage of the cell can causes by direct interaction to the cells by electron, proton, alpha particles, or indirect means by photons (X-ray or gamma-ray) [17]. The effect includes; a physical effect that causes transfer and abortion of energy causes the ionization and excitation of the molecules, which is associated with the biophysical effect. The chemical and biochemical effect includes the production of free radical and polymerization and depolymerisation reaction which is responsible for damage of cells and breaking down of DNA is associated with the biological effect of radiation [17].

1.3. Fractionation for Head and Neck cancer in radiotherapy

Fractionation in radiotherapy refers to the use of a small amount of radiation dose as a fraction of the total prescribed dose. Fractionation radiotherapy has an advantage over conventional RT for both overall survival (OS) and locoregional control (LRC) [18]. Various fractionation schedules are introduced based on a better understanding of R's of radiobiology; repair, repopulation, re-oxygenation, redistribution, and fifth R as radiosensitivity. Advancement in radiobiology introduced other fractional schedules; hyper fractionation, hypofractionation, accelerated

fractionation, alter fractionation. All these unconventional fractional are different in terms of dose per fraction and time [18]. Conventional fractional schedules include 1.8 -2 Gy per fraction becomes convenient for both local control and normal tissue complications.

Conventional fractionation schedules for H&N cancer used 2 Gy per fraction in a single day up to 70 Gy including lymph nodes [19]. Due to the repair of some rapidly proliferate cells between two fractionation schedules, alter fractionation can be the alternative and deliver twice per days with minimum fractionation to potentially reduced the late toxicity, which allows delivering the higher total dose than conventional fractionation schedules and the accelerated radiotherapy where 1.8 Gy to 2 Gy twice in a day or more than 5 fraction per week to reduce the overall treatment time [18].

Hyper fractionation uses a small amount of radiation dose with a larger fraction. In contrast, Accelerated fractional required less amount of time by delivering more doses in a single day. Meta-analysis of head and neck cancer reported for advanced H&N cancer treatment implies the combination of hyper-fraction with chemotherapy is a suitable option and concluded that the altered fractionation schedules improved the overall survival rate [20]. The study of Accelerated Hyper fractionated Radiotherapy (AHRT) versus Conventional Fractionation Radiotherapy for H&N Cancer and concluded the AHRT shows superiorities over conventional fractional with improved overall survival (OS) and Locoregional control (LRC) [21].

1.4. Medical linear accelerator

The schematic diagram of the medical linear accelerator is shown in figure 3.

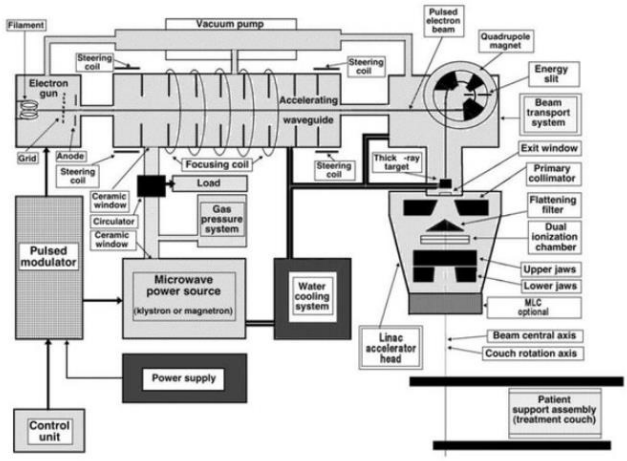

Fig. 3. Schematic diagram of medical linear accelerator [22]

The development of the medical linear accelerator has been started from the late 1950s to now and modern accelerators can operate in dual-energy mode (electron and photon). The complex design of the linacs is associated with the hardware and software components which allow delivering more accurate and precise radiation beam.

A multi-leaf collimator (MLC) is an important component of linacs for beam shaping. MLC is the leaf pairs and is mounted on the linacs head. The movement of individual multi-leaf is based on computer control, which allows delivering the dose by changing each leaf pattern during irradiation. This feature becomes a milestone for the introduction of complex dose delivery techniques; IMRT and VMAT. Customized blocks also are used for beam shaping it needs to manufacture for an individual patient and each field; as a result, they are replaced by MLC, which reduced the overall treatment duration [23].

The modern linear accelerator is manufacture by various companies and is available in the market. Accuracy Tom therapy™, Elekta Unity™, and Varian Halcyon™, etc. are linear accelerator models that are capable of producing multi-energy photon 6 MV, 10 MV,16MV, and 18 MV. Using the higher energy photon has the advantage of a lower entrance dose but a higher exit dose. Generating the neutron from the target is an issue with selecting the higher energy photon and can expose with patient causes secondary cancer. For IMRT and VMAT, photon energy is generally suggested not exceeding 10 MV to avoid the generating of the neutron [23].

Linacs attached with imaging modalities have a significant advantage in radiotherapy also called image-guided radiotherapy (IGRT). On-board imaging KV CBCT has an advantage for patient setup and its application is widening though it has poor image contrast for soft tissue. To reduce this problem MR based linacs are introduced and can perform better image contrast resolution with the application of magnetic field [23].

For better clinical use of an accelerator, several quality assurances and Quality control tests are performed to check the linacs performance within the tolerance limit. Guideline for the various test was reported by AAPM TG-142 for "Quality assurance of medical linear accelerator" and TG-100 for the "Application of Risk Analysis Methods to Radiation Therapy Quality Management" [24]. The depth dose of various photon energy in water is tabulated in table 1.

Table 1. Depth dose in water for different photon beam [23]

Parameters	**Co-60 80 SSD**	**Cobalt-60 100 cm SSD**	**4 MV photon 100 cm SSD**	**6 MV photon 100 cm SSD**	**10 MV photon 100 cm SSD**	**15 MV photon 100 cm SSD**	**18 MV photon 100 cm SSD**
Depth of maximum dose	0.5 cm	0.5 cm	1 cm	1.5 cm	2.3 cm	2.9 cm	3.2 cm
Percentage depth dose at 10 cm depth	56.4%	58.7%	63.0%	67.5%	73.0%	77.0%	79.0%

Depending on the types of treatment modalities energy of the X-ray beam is classified as:

- Superficial X-ray (20-120 keV). These low-energy X-ray has a penetration depth of up to 5 mm and is applicable for the treatment of skin cancer [25].
- Orth voltage X-ray (200-500 keV). Penetration depth is up to 6cm and is used for skin, superficial structure, ribs, etc.
- Megavoltage X-ray (1-25 MeV). This energy of x-ray has more penetration power and less attenuated by surface structure and can cause more biological effects than low energy x-ray [25]. This range of X-ray energy is used in the treatment of tumours located deeper including head and neck cancer.

1.5. Advanced Treatment modalities for head and neck cancer

1.5.1. 3-D Conformal radiotherapy

Introducing 3D imaging modalities; computed tomography (CT) and magnetic resonance imaging (MRI) in radiotherapy have a paradigm shift in radiotherapy irradiation technique. Treatment planning and delivery based upon the 3D images from CT and MRI leads to the better delegation of target volume and organ at risk (OARs) and nearby tumours [26, 27]. Forward treatment planning with a three-dimensional structure can perform better target volume coverage and reduced the toxicity to the normal organ [28]. 3D CRT is a convenient technique for the treatment of head and neck cancer where advanced treatment modalities like IMRT, VMAT are not clinically possible to implement. It is easy to implement and not required advanced treatment planning as IMRT and VMAT [29]. Uniform fluence of radiation dose to the target and critical structure and large no of tissues are exposed with the high radiation dose is an issue concerned with 3D CRT.

1.5.2. Intensity-modulated radiotherapy

Advancement in radiotherapy technique from 3D CRT to intensity-modulated radiotherapy (IMRT) leads to the significant improvement in better PTV coverage and normal tissue sparing [30]. Multi-leaf collimator (MLC) modulates radiation beam by using computer control optimization algorism to shape beam into desire dose distribution along with the inverse treatment planning which increases the dose to the target volume compared with 2D RT and 3D CRT is a vital aspect of IMRT [31]. In IMRT, the beam can be delivered with (1) static or using Multi-leaf or VMAT [32]. Advantage of IMRT to treat head and neck cancer due to its uniqueness of concave target shape along with better spearing of normal tissue; salivary glands, esophagus, optic nerves, brain stem, and spinal cord and delivery of high radiation dose to the hypoxia for locoregional control (LRC) [33]. The disadvantage of IMRT over 3D CRT is missing the target volume due to its steep dose gradient and high conformity index [34].

Ehab M. Attalla et al, [35] demonstrate the dosimetry comparison of IMRT and 3D CRT for head and neck cancer shows the better dose distribution of IMRT with CTV than 3D CRT along with reduction of dose to the critical organs; parotid, brain stream, and spinal cord.

Another study was carried out by XS Wang and A Eisbruch et.al, 2016 [36] for head and Neck cancer using IMRT to minimize the radiation damage to the salivary gland within the oral cavity which leads to dysphagia and xerostomia (dry mouth) and conclude that xerostomia can be reduced by limiting the mean dose to the gland. Gupta et al [37] studied the long-term outcome and radiation-related morbidity with IMRT vs 3D CRT for head and neck squamous cell carcinoma shows the superiority of IMRT for reducing late morbidity of radiation.

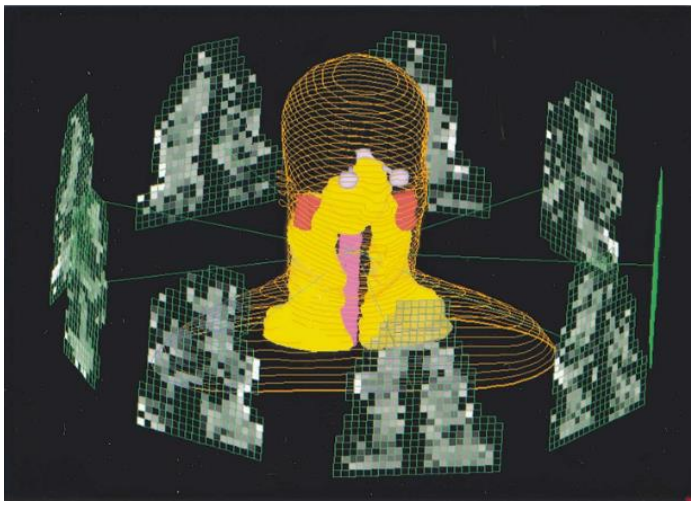

Fig. 4. Intensity-modulated radiotherapy [38]

1.5.3. Volumetric modulated arc therapy

Volumetric modulated arc therapy **(**VMAT) is a novel irradiation technique, can deliver conformal dose with variable gantry speed along with the movement of a Multi-leaf collimator. In fact, In VMAT, gantry speed, varying dose rate, continuously changing Multi-leaf collimator shape during dose delivery along with modulated beam intensity is a key aspect of VMAT [39, 40]. These degrees of freedom enhanced to achieve less toxicity and enhance the biological effect and increased the capability of beam intensity modulation concerning IMRT. VMAT has gained momentum as IMRT in terms of less no of monitor unit used and overall reduction of dose delivery time which leads to the reduction of intra-fractional error and more no. of the patient can be treated in oncology centre [41, 42, 43].

To achieve VMAT delivery specific medical linear accelerator with variable dose rate (VDR-VMAT) and advance treatment planning system is required and is significantly costly concerning constant dose rate VMAT, though it required specified TPS [43]. Indeed, VMAT with simultaneous integrated boost (SIB) allowed delivering different doses to the different target volumes, which significantly reduced the dose to the normal tissue [44].

Commercially available, Halcyon linacs (Varian Medical Systems, Palo Alto, CA) combined with flattering free filter (FFF) beam with higher efficient leaf and gantry speed with compared to c-arm linacs have clinically advantage for achieving dose delivery of time efficiency. S. Michiels et al [45] studied the comparison between O-arms linacs (Halcyon) and C- arms linacs in terms of

plan quality and delivery time for head and neck cancer and reported that better plan quality of two arches over C-arms along with reduction on time for image acquisition and plan delivery [45].

Sanjib Gayen, et al [46], studied the dosimetry advantage of non-coplanar VMAT plan has advantage on better target coverage and spearing OARs for head and neck cancer. In contrast coplanar overall increase no of monitor unit, delivery time, uncertainty with patient positioning. Several studies were carried out for comparison between IMRT and VMAT dose delivery technique for overall treatment delivery time for head and neck cancer and found that the overall treatment time for VMAT is significantly reduced than IMRT.

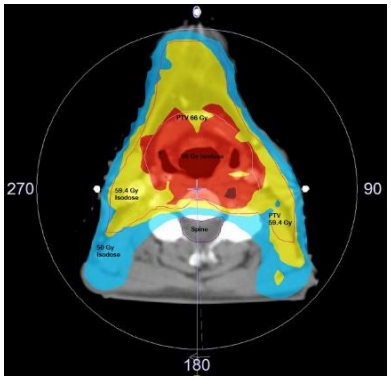

Fig.5. Single arch VMAT technique [47]

1.5.4. Image-guided radiotherapy

Image-guided radiotherapy (IGRT) used advanced imaging modalities during the highly conformal radiation therapy for reduction of geometric uncertainty and high precision during treatment. The clinical advantage of IGRT is when the tumour is close to the critical organs and the tumour control level exceeds the normal tissue tolerance [48]. IGRT along with IMRT, VMAT, and Stereotactic techniques has a significant contribution to precise dose delivery along with reduction of radiation-related morbidity [49, 50]. Its clinical significance is more in the particle therapy, physical nature of Bragg peaks, where more accurate target positioning is required. In contrast, time-consuming and additional exposure to radiation is a drawback concerned with IGRT [51, 52].

The image-guided system is involving in the ionizing and non-ionizing based imaging system which includes; ultrasound, MRI, optical tracking system, Electromagnetic Tracking Systems, Electronic Portal Imaging Devices (EPID), Cone Beam CT (CBCT), kV or MV, Fan Beam (kV, MV) CT, and Hybrid Systems for Real-Time 4D Tracking, etc.[52].

IGRT is applicable for tracking the shrinking of tumour size after some fraction of radiation, variation in counter due to weight loss, rapidly proliferation tumour cell between treatment session and can be replanted based upon these parameters, also called adaptive radiotherapy [53, 54].

A. Navran et al [55], documented the IGRT applicable for the VMAT for Head and neck cancer focus for the margin reduction and toxicity and its result shows that the CTV_PTV margin reduction in 5 to 3 mm minimized the radiation-based toxicity.

1.6. Dosimetry for external beam radiotherapy

Dosimetry is the measurement of radiation dose in a medium by ionizing radiation in terms of absorbed dose. Dosimetry is essential in a clinical application where irradiation in the human body is determined in terms of absorbed dose in water [56]. It is measured in a quantity called Gary (Gy) (J/Kg) and is directly related to the biological effect.

The accuracy in dose delivery recommended by ICRP (international commission of radiation unit) is within the ±5 %. However, some advanced irradiation techniques need stick requirements than this recommended value. The number of codes of practice has been published specially target for the high energy photon and electron beam by the various physicist. Advancement in dosimetry protocols given by IAEA, AAPM TG-51, and ICRP (International commission of radiation unit) are clinically implemented for absorbed dose verification [57, 58].

The effect of ionizing radiation in the human body is not only completely described by the absorbed dose but also includes the radiation and tissue-weighting factor, which are associated with the radiation-induced effect (static and deterministic effect) [58]. The deterministic effect is directly related to the absorbed dose and the severity of the effect increases with dose and is called the non-stoic effect. The Tissue weighting factor for various tissue is given in the table. The tissue weighting factors for the different organs are presented in Table 1.

Table 2. The tissue-weighting factor for different tissue [59]

Tissue (organ), T	**Tissue (organ) weighting factor,** W_T
Gonads	0.20
Bone marrow (red)	0.20
Colon, Lungs, stomach,	0.12
Bladder, chest, liver, oesophagus, Thyroid gland	0.05
Skin, Bone surface	0.01
Adrenals, brain, small intestine, kidney0.05muscle, pancreas, spleen, thymus, uterus (the weighting factor 0.05 is applied to the average dose of these organs)	0.05

1.6.1. Relative dosimetry

Relative dosimetry quantifies the measurement of absorbed dose in a medium with the calibration of the dosimetry system. The most commonly used Relative dosimetry systems are radio chromic film, TLDs and these dosimeters need an additional process to measure the dose, are called passive dosimeter. It is used for acceptance testing and periodic quality assurance testing of a linear accelerator.

1.6.2. Absolute dosimetry

Absolute dosimetry systems are based upon the direct measurement of absorbed dose in a given radiation field without the need for calibration on it. Absolute dosimetry systems are;

- Calorimetric dosimetry: It is based upon the direct transformation of energy from ionizing radiation to the dosimetry media.
- Chemical (Fricke) dosimetry system: Fricke-based dosimetry is regarded as the primary standard dosimetry. When an ionizing radiation hits on the chemicals it converts ferrous ions ($Fe^{2+)}$ into the ferric ion (Fe^{3+}) by oxidation on ferrous sulphate solution.[60]
- Ionometric dosimetry system: Used to measure the dose in the form of charge generated by ionizing radiation in a medium. An ionization chamber is used as both an absolute and relative dosimetry system

  The commonly used dosimeter in photon therapy is discussed in the subsection below.

1.7. Ionization chamber

An ionization chamber is a crucial component in radiation dosimetry used in external beam radiotherapy; x-ray and CO-60 source. It is the one-dimensional representation of the dosimetry system which consists of a chamber with graphite rode as a central collecting electrode and the chamber is filled with a gas [61]. The ionizing radiation ionized the gas molecules into positive and negative ions, the charge is collected by applying the potential and measured in the form of current.

Depends upon the types of application (energy of the beam) it is categorized into two types; cylindrical and parallel plate. Cylindrical ion chamber also called thimble types chamber and used in high - energy photon beam and parallel plate chamber for low energy photon beam. The volume of the ion chamber is varied and is depends upon the types of application such as small field size, low dose rate region, etc. [61].

According to protocol 398 [63], a cylindrical ion chamber is applicable for beam calibration as a reference instrument, cross-calibration, or routine measurement. For the calibration of a high-energy photon beam, an electron beam with energy above 100 MeV, and particle radiation mainly proton and the heavy ion beam is performed in a water phantom. The typical collecting volume of the chamber should be between 0.01 cm^3 to 1 cm^3. The alignment of the ionization chamber is in such a way that radiation fluence is uniform for chamber cross-section and its design equilibrates with ambient temperature and pressure.

The plane-parallel ion chamber is recommended for the reference dosimetry for both photon and particle beam if it is calibrated in terms of absorbed dose in water. Chamber is constructed as water equivalent as possible and used in dose measurement in solid phantom.

A waterproof sleeve for the chamber is needed if it is applicable for the absorbed dose measurement in water and is made from the PMMA and the thickness of the wall is less than 0.1mm which is helps to mention the thermal equilibrium. The chamber should be calibrated with or without a sleeve. Chamber is open type it is exposed to the environment directly so that correction factor due to temperature, pressure, and humidity should be taken into the account [63].

According to the IAEA TRS-398 and TG-51, the ionization chamber is applicable for both absolute and relative dosimetry. To measure precise dose measurement of ion chamber for high energy

photon beams different correction factors are taken into account; Temperature pressure correction factor ($k_{T,P}$), chamber calibration factor ($ND,w.$), ion recombination correction factor(k_S), Beam quality conversion factor.

Temperature pressure correction factor ($k_{T,P}$) is applied if the temperature, pressure is fluctuated than standard condition (20°C and 101.3 kPa) and is corrected by using formula;

$$k_{T,P} = \frac{273.2+T}{273.2+T0}\frac{P0}{P} \quad (1)$$

Where, T0, P0, and T, P are the standard temperature pressure and are the measured value of temperature and pressure.

The polarity effect of the chamber is calculated using the following expression;

$$Kpol = \frac{|M+|+|M-|}{2M} \quad (2)$$

Where**,** M+ and M- are the electrometer reading with positive and negative polarities and M is the reading with routinely used polarity.

Ion recombination factor (k_S) is due to the incomplete collection of charge due to the low applied ion potential.

1.8. Gafchromic film

A type of Radio chromic film is regarded as a 2D dosimeter and its increasing therapeutic application with its special characteristics such as; high special resolution, higher sensitivity, low energy dependency, high accuracy under dynamic measuring conditions, and nearly water equivalence materials [64, 65]. These features of films become significantly important for dosimetry in diagnostic radiology, nuclear medicine, radiotherapy including particle radiation (proton and heavy ions) [65, 66]. Film dosimetry is considered for applicable tools as reference dosimetry for in-vivo dosimetry as an alternate of metal oxide semiconductor field-effect transistor (MOSFETs) [67].

The image formation process for Gafchromic film is the post-irradiation of the sensitive materials (lithium-10, 12- pentacosdiynoate – LiPCDA) after irradiation [68]. The colour of the film is changed into dark blue due to polymerization within sensitive materials and the darkness level relies on the absorbed dose [66]. The film response is measured by densitometer and scanner by taking optical density before and after irradiation. The optical density depends upon the orientation of the film during the scanner therefore, it is very crucial to use consistent orientation [68].

Due to some drawbacks of the first introduced radio chromic film application in radiotherapy dosimetry in its sensitivity, uniformity, and cost-effectiveness. The development of radio chromic film for the external beam radiotherapy (EBR) with sensitivity and uniformity has introduced in 2004 and its application has been a significant increase over silver halide radio chromic film. After

precious study of EBT film leads to the further development of EBT2, EBT3, and EBT-XD with improved sensitivity, uniformity, and special resolution in 2009, 2011, and 2015 respectively [68]. The configuration and composition of the EBT, EBT-2 and EBT-3 film models are shown in figure 6.

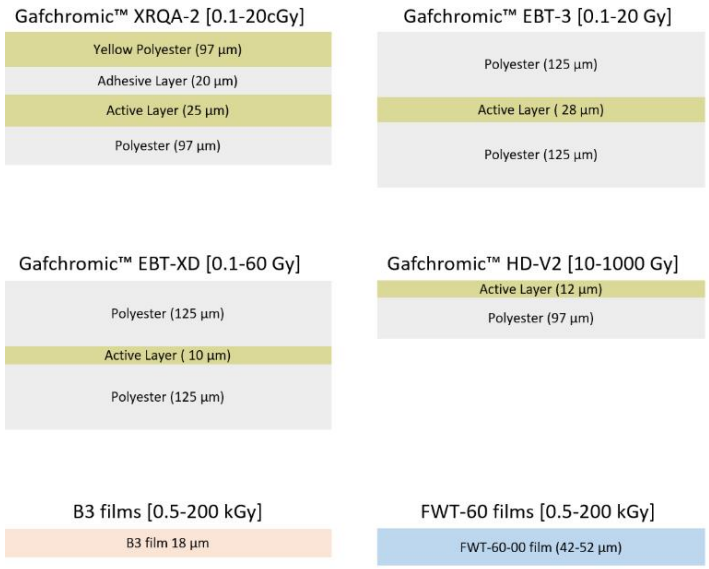

Fig. 6. Configuration and dynamic range of radio chromic film [69]

The energy range of film depends upon the film models, manufacture, and sensitivity. The active layer of the film is sandwiched between the plastic substrate with different thicknesses and it depends upon film type. GafChromic film EBT series are applicable for absorbed dose measurement in advanced radiotherapy techniques in external beam radiotherapy; IMRT, VMAT, proton therapy with small field sizes and steep dose gradient regions [68].

The optical density measured the dose-response of the film, when irradiated with ionization radiation, is expressed in terms of optical density and measures the change in optical density before and after irradiation [69]. Mathematically optical density is.

$$\mathrm{OD}\ (\lambda) = \log \frac{I_o}{I} \tag{3}$$

Where I_o is intensity before irradiation and I, the intensity during irradiation.

1.8.1. Temperature and humidity dependence

The RCFs are sensitive to temperature and humidity so that their response to irradiation can be an influence. One of the major advantages of the film is its stability with temperature up to 60°C, and easily handled with ambient light for short period. During the calibration and practical use, the response of the film in the environmental condition is taken into the account and corrected [68].

1.8.2. Post irradiation stability

The time duration of polymerization within active components of film (deacetylate) occurs in few milliseconds. RCFs model like HD-810 and MD- MD-55 with active components PCDA irradiated with gamma radiation it takes 100 μs of irradiation to appears polymer. The early film types s (HD-810, MD-55, HS, MD-V2-55) need a few weeks to stabilize which leads to growth in optical density with time. For RCFs EBT models polymerization is faster within 24 hours of post-irradiation [68]. For EBT3 models increase in optical density by only 2.5% between 24 hr and 16 days after post-irradiation. Measure uncertainty relatively decreases after 24h of irradiation and has very little impact on dosimetry measurement [68].

1.9. Thermoluminescence based dosimetry system

TLDs are regarded as a 2D dosimeter and are suitable for point dosimetry due to their small size used for in-vivo dosimetry and phantom. TLDs are characterized as; small, reusable, easy to handling and it is available in small size and TLDs are available in different form; in ships, power, ribbons, and rods [71]. Various materials are used for the production of TLDs however; the most commonly used one is lithium fluoride [72].

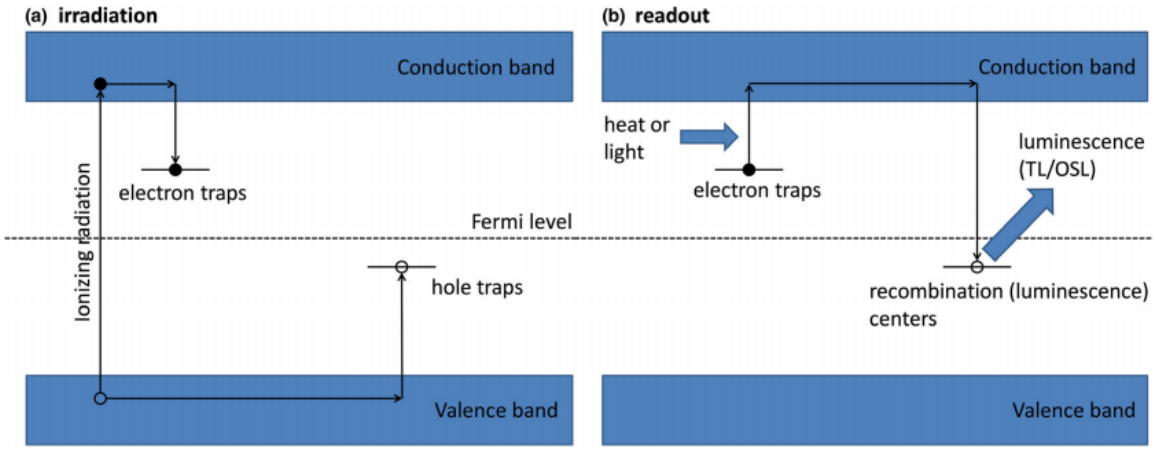

Fig. 7. (a) Energy level diagram of luminance and (b) readout process [72]

When the TLDs materials are exposed to the ionizing radiation, ionization in TLD materials promotes the number of an electron to jump into the conduction band, leaving vacant space in a valence band. These charges can freely move or stay in the energy trap region, created by the process of doping impurities. During the simulation process, the electron is released from the trap region and recombine with the hole with creating the hole in the excited state. During the process of returning to the ground state, a photon of light is emitted. The readout process is done by using a photomultiplier tube, which converts visible light quanta into charge particle and is measured in terms of count per unit time. AAPM TG-191 provided a brief description of the clinical application of luminance dosimeter (TLDs and OSLDs) [72].

Commonly used TLD 100 dosimeter and is based upon the lithium fluoride shows the close tissue equivalent, dose range (10 mGy-10 Gy), and high sensitivity, precision and shows the superliner behaviour of TLDs over 10 Gy in photon beams.

One of the major drawbacks associated with real-time readout with TLDs due to its post-irradiation processing which replaces the TLDs with diode even it is applicable to measure the skin dose. The figure represents the glow curve of LiF: Mg, Ti (TLD-100) which represents the different peaks concerning the temperature. Peaks corresponding to 200–225°C temperatures are regarded as the best dosimetry application with stability at room temperature. Lower peaks are unstable at room temperature for shallow trapping depth [72].

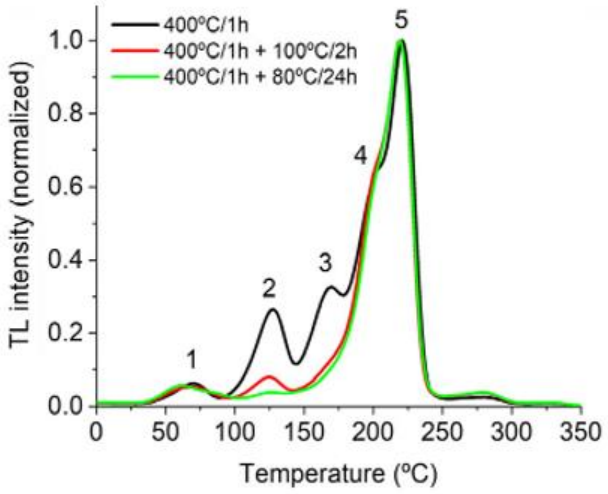

Fig. 8. Thermoluminescent curves of LiF: Mg, Ti (TLD-100) peaks corresponding to the trapping centre [72]

1.10. Gel dosimetry

Due to some limitations of one-dimensional (ionization chamber), Two-dimensional (radio chromic film) dosimeter used in clinical application. Gel dosimeters are introduced as three-dimensional for complex dose distribution for advanced radiotherapy techniques such as; IMRT, VMAT, IGRT, and quality assurance [73]. One of the major advantages of gel dosimeters is applicable for both phantom dosimetry and as a dosimeter [73]. Fricke chemical and polymer-based are the two categories of gel dosimeter. These gels are made from tissue-equivalent materials, which show similar radiation interaction properties for a wide energy range [73]. The sensitivity of gel causes the colour change when exposed to the ionizing radiation and the darkness of the colour increases the dose. The composition of the gel can be modified depends upon the application and are applicable for all types of radiation photon, electron, neutron, and proton [74].

Fricke chemical dosimeter contains the ferrous sulphate solution. Once the solution is irradiated, the transformation of ferrous ion (Fe^{2+}) into the ferric ion (Fe^{3+}) is due to oxidation. It provides a less spatial resolution due to the diffusion of Fe^{3+} ion, the time laps for both irradiation and

measurement. The various gelling agent was introduced to remove the diffusion in Fricke gel but not significantly successes, which limit its clinical application [75].

Introducing the Polymer-based dosimeter overcomes the diffusion rate of Fricke gel dosimetry but it has its limitation for atmospheric oxygen can cause the polymerization reaction. This causes the manufacturing of polymer gel more complex. Polymer-based dosimeter has an advantage over Fricke on spatial resolution and stability [74].

Minsk Lee et al [73] study the application of gel dosimetry for the development of patient-specific 3D printed phantom applicable for liver cancer radiotherapy using patient CT images and shows the validation of dose distribution. Baldock et al [76] also present their ideas of gel dosimeter is used as an end-to-end quality assurance for magnetic resonance-based linacs.

1.11. Phantom for external beam radiotherapy

Phantoms are used in radiotherapy for dosimetry verification by measuring the absorbed dose in a medium for the verification of the treatment plan. Following the Protocols TRS-398 [71], Phantom should be made from water or water equivalent materials such as; PMMA, polystyrene and shows similar absorption and scattering properties as water. Depending upon the types of application phantom are made from different materials, shapes, and sizes. Moreover, the other types of phantom-like solid-state or anthropomorphic are made with the similar shape, size, and body as the human tissue or structure and made from the materials, which show similar radiation characteristics as the tissue or organs [77].

Different phantoms water phantom, solid-state phantom, Voxel phantom, slab phantom and, an anthropomorphic phantom are used in clinical practice for verification of treatment plan, reference dosimetry, routine quality assurance, and quality control process [78]. Some of the commonly used phantoms are discussed below.

1.11.1. Water phantom

According to the TRS-398 protocol [62], Water is regarded as the reference dosimetry for both photon and electron beam. The physical shape of the phantom looks like a cube along with a dosimeter that can be placed and made from plastic materials. It acts as the homogeneous medium where the absorbed dose can be measured. The shape and size of the water phantom are depended upon the energy of the photon beam. According to the IAEA and TRS- 398 and TG-51 [79], water phantom is recommended as the reference medium for absorbed dose measurement for photon beam and calibration of ionization chamber (cylindrical and plane-parallel).

The recommended water phantoms should be “The water phantom should extend at least 5 cm beyond all four sides of the largest field size employed at the depth of measurement.” [80].

Fig. 9. Water phantom for absorbed dose measurement [81]

1.11.2. Solid-state phantom

Solid-state phantoms are made from materials with a density equivalent to water and show similar abortion and scattering properties as water. ICRU Report 44 present the uncertainty for the calculation of absorbed dose is not exceeding 1% [82]. For the selection of materials used in megavolt photon energy, relative electron density (RED) of a material is taken for the comparison of water equivalent properties. These are generally, PMMA, solid water, virtual water, plastic water, and these follow the requirement for low energy X-ray and electron beam [62]. Plastic phantom is not generally recommended for the reference dosimetry due to the uncertainty that arises for measuring absorbed doses due to the difference in density of plastic to water medium [84]. Water phantom is more time demanding for the routine beam check. Therefore, the water-equivalent plastic phantom is more practically applicable for the routine measurement and dose verification for the advanced radiotherapy technique IMRT, VMAT, IGRT [83].

Fujio Araki et al [84] study the homogeneous slab phantom made from the plastic materials name as solid water high equivalency (SWE) with water equivalent physical properties; mass and electron density and used as a substitute of water phantom for routine dosimetry and treatment plan verification for high energy photon beam. The standard PMMA phantom block along with the sleeve for the position of the ionization chamber is shown in the figure.

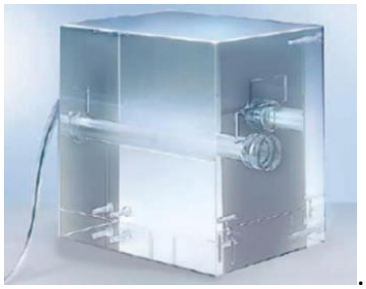

Fig. 10. Standard PMMA phantom [85]

1.11.3. Anthropomorphic phantom

Most of the anthropomorphic phantom designs are based on the reference represented by ICRP report 23 and 89 (1975, 2002) [86]. The development of the phantom is based upon the shape, size, application areas, materials types, and anatomical structure of the organs. The more complex structure needed the complex model to generate [88]. The important parameters that need to be

taken into account are the density of the materials is the same as the cross ponding organ density, scattering and absorption properties, and reproducibility of the phantom materials [88]. The anthropomorphic phantom is classified into two different types; computational and physical anthropomorphic phantom.

1.11.4. Computational anthropomorphic phantom

Computational anthropomorphic phantoms are based upon the computer models that represent the human anatomy structure and different organs and are applicable for calculating absorbed dose distribution for validation of treatment planning [89]. These computer-based phantom are categories into two Stylized phantom and Tomographic (Voxel) phantom.

Stylized phantoms have a significant contribution to dosimetry verification. It provides the approximation of true human anatomical features including internal structure based upon the mathematical equation. The first stylized phantom was introduced in 1969 as a medical internal radiation dose and later on followed by the male, female, and pregnancy phantom for the absorbed dose verification [89, 90]. Its clinical application areas are widening from diagnostic radiology, radiotherapy, and nuclear medicine. Its superiorities over tomographic phantom in terms of flexibilities of shape and size.

Tomographic phantom is also known as voxel phantom represents the 3D information of the human anatomy as a 3D array of volume elements and is reconstructed based upon the 2D slices from imaging modalities such as; magnetic resonance imaging (MRI) and computed tomography (CT) [90]. Due to the advancement in tomographic phantom, its development is widening in its range including; male, female, and paediatric, pregnant women phantom for dosimetry verification. These two figures 12 (a) and (b) represents the whole body computational stylized phantom and tomographic phantom with the women having different pregnant periods respectively.

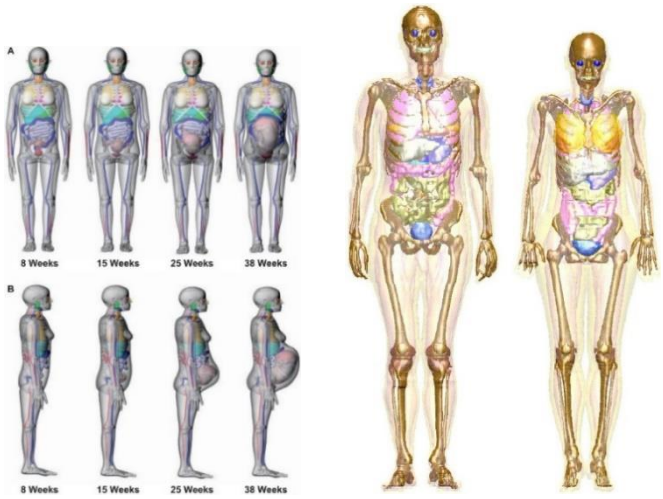

(a) (b)

Fig. 11 (a) Computational anthropomorphic phantom [91] (b) Voxel phantom of pregnant women [92]

1.11.5. Physical anthropomorphic phantom

Physical anthropomorphic phantoms are designed based upon the representation of human anatomy and made from materials that show similar radiation interaction properties (scattering and attenuation properties) on a tissue to determining absorbed dose for specific tissue or organ. In addition, it has the same electron density, effective atomic number, and tissue inhomogeneity as human organs [87]. These phantoms are divided into the different coronal planes where dosimeters (TLDs, ion chamber, films) are inserted to measure an absorbed dose.

The development of the anthropomorphic phantom has been started in 1906, based on the dosimetry of tissue-equivalent materials applicable for an alternative for absorbed dose measurement in the irradiated organs. Later on, Water and wax have introduced as the alternative materials for the muscle and soft tissue, and it was found that it is a significant discrepancy between the attenuation coefficient of muscle and soft tissue with that wax at low photon energy. Later improved wax-based phantom with high atomic no. was implemented and has significantly applicable in dosimetry for long period. Dosimetry of wood-based phantom is also taken as dosimetry research but its application is limited due to its high attenuation properties of the wood [88]. Later on, the development of the phantom is not only focused on radiotherapy but also radio diagnosis, radiation protection in imaging, etc.

The advancement of printing technology, as well as the availabilities of printing materials which are applicable for clinical dosimetry, leads to the development of 3D printing in medical application. Due to the limitation of availabilities of 3D printing materials, the selection of printing materials is based upon the closest CT Hounsfield unit corresponding to equivalent tissue [93]. Now a day's different physical anthropomorphic phantom for male, female, paediatric as well as various organs such as; head and neck, breast, brain, thorax, and whole-body phantom are commercially available. The figure below represents the different types of physical anthropomorphic phantom.

Fig. 12. Different Anthropomorphic phantom [94]

N. Kadoya et al. [95] study the possibilities of the 3D printed head and neck phantom and successfully constructed with tissue equivalent materials for soft tissue was Polylactide due to its acceptable CT values and bone structure for higher density materials plaster with 2.3 g/ cm^3 for the effectiveness of the phantom materials were evaluated with by comparing phantom CT with a

patient for soft tissue and bones. The dose distribution of phantom and patient CT images was compared as shown in the figure.

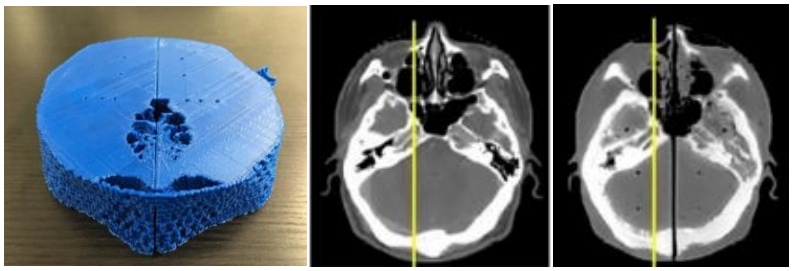

Fig.13. Head and neck slab phantom, Patient CT images, Phantom CT images [95]

Grehn et al [96] carried out study for the dose distribution for H&N cases with dental fillings with the specific phantom. The study mainly focused on metal artefacts for a dental filling. Phantom was contracted with tissue equivalent materials with physical characteristics such as attenuation coefficient and cost-effectiveness. These phantoms are applicable for effective treatment planning with dental filling with head and neck radiotherapy.

Fig.14. Phantom for head and neck with a dental filling [96]

Steinmann et al [97] studied the development of anthropomorphic H&N phantom for MR-guided radiotherapy applied for end-to-end quality assurance. Phantom was constructed with an acrylic shell with a custom insert that mimics the organs at risk and target structure. The primary and secondary PTV was constructed with synthetic Clear Ballistic gel and OARs with acrylic. The dose distribution was measured by using TLDs and EBT3 radio chromic film and the result of reproducibility and feasibility testing indicate the clinical application of Phantom as a Quality assurance tool. Bao et al [98] studied the Comprehensive end-to-end test for intensity-modulated radiation therapy for nasopharyngeal carcinoma using an anthropomorphic phantom and EBT3 film to evaluate the accuracy of the treatment plan. The phantom was not limited to radiotherapy but also the imaging modalities. Alqahtaniet al. studied the developed anthropomorphic phantom with reproducible, Flexible, and cost-effective tools for the gamma camera for the H&N region.

Abbasid S. et al [99] carried out the comprehensive study, by modelling the new types of anthropomorphic phantom applicable for the verification of dose distribution for head and neck radiotherapy also including the absorbed dose received by ears, eyes, optical nerves, etc.

This phantom is made from polylactide (PLA) with physical dimensions 23×24×32 cm^3 and clinical application for high-energy photons with energy greater than 10 MeV for brain tumours

shows less attenuation. The study concludes that the phantom can be used for multiple purposes like evaluating dosimetry of organs at risk for ears and eyes and dosimetry verification of treatment planning system. The anatomical structure of ears and eyes regions can be replaced with TLDs to measure point dose and the brain parts can be filled with a gel dosimeter to get the 3D dose distribution.

Fig. 15. General Overview of head and Neck phantom [99]

1.12. IAEA dosimetry audit overview

Science 1969 IAEA/WHO implemented the postal dosimetry service for various radiotherapy centres for beam calibration in radiotherapy to reduce the uncertainty in the radiotherapy process. The service was first started for the cobalt-60 unit and later on, extended for the high-energy photon beam produced by a medical linear accelerator [100, 101]. IAEA introduced the national dosimetry audit program Coordinated Research Projects (CRP) for various time intervals was introduced to its member state. First CRP is based upon the beam calibration in reference condition entitled on "Development of a Quality Assurance Programme for Radiation Therapy Dosimetry in Developing Countries".

Non-reference condition-based audit methodology as second CRP was TLDs-based audits, which can assist for the individual radiotherapy centre for independent dosimetry performance. "Development of Quality Audits for Radiotherapy Dosimetry for Complex Treatment Techniques" as a third CRP, is targeted for the advanced irradiation technique conformal with MLC and heterogeneous target volume [102]. Final CRP project for more advanced irradiation technique IMRT for end-to-end verification included in every chin of radiotherapy from image acquisition to dose delivery and additionally for the MLC positioning checking.

A remote End-to-End audit methodology was developed by IAEA CRS for complex dose delivery technique IMRT/VMAT applicable to test every step in radiotherapy procedures. A solid phantom made from polystyrene with a density of 1.040 gm / cm^3 with PTV, OARs are 8mm apart, and dosimeters TLDs and EBT3 can be inserted on it. The figure below represents the solid-state polystyrene slab phantom for IMRT/VMAT QA [103].

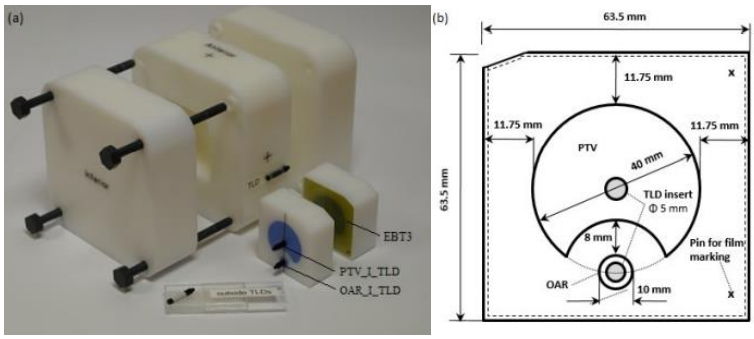

Fig. 16. Solid slab phantom for IMRT QA inserts and cross-section image of phantom [104]

On-site audit methodology was developed by IAEA for IMRT/VMAT for Head and Neck as End-to-end testing which can be used for verification of every step involved in the radiotherapy process including dosimetry, treatment planning, and dose delivery [105]. An anthropomorphic phantom with target volume and organs at risk was defined and respective dose constraints were provided. The ionization chamber and the film can be inserted for the absorbed dose verification in predefine location by comparing with the dose provided in TPS. These audit methodology data gather and multicentre study can be performed for the inter-comparison of results among the various centre for the quality of treatment with IMRT to achieving the best radiotherapy outcome.

1.13. Summary of theoretical overview

Numerous studies were carried out regarding the dosimetry aspect of megavolt (MV) photon beam with advanced irradiation technique IMRT/VMAT for H&N cancer. Due to the complex anatomy of this region and the more complex proximity of the critical organ, it needs a more demanding dosimetry protocol for the verification of the treatment plan. Ion chamber, film, TLDs dosimeters are used to measured absorbed dose in respective anatomy structure.

Various dosimetric phantoms are implemented for the dose determination for critical organs. The most commonly used dosimetric phantom systems are water phantom, solid-state, Voxel, slab phantoms. These phantoms are limited in their application in the radiotherapy process due to their shape, size and are made from homogeneous materials. However, an anthropomorphic phantom can provide a better dosimetry output due to its radiation attenuation characteristics such as heterogeneity, which is similar to the composition of human tissue. Various research studied its application for patience specific quality assurance, end-to-end testing shows the applicable tools in the radiotherapy process.

The SHANE phantom presents a novel methodology for dosimetry in the clinical setting whereby it reproduces more accurate dose profiles for head and neck tumours that are situated close to critical organs compared to other phantoms.

2. Materials and methods

The experiment was performed in Siauliai Hospital Department of radiotherapy using linacs. Elekta infinity and Onkologinė ligoninė, Volungių g. 16, Kaunas with Halcyon Varian medical linear accelerator.

2.1. Materials used:

- phantom SHANE,
- Ionization chamber (PTW 30013-2703),
- Electrometer (T10002 UNIDOS),
- Linear accelerator (Electra infinity),
- Octavius 729 Detector,
- Linear accelerator (Elekta infinity and Halcyon),

(a) (b)

Fig. 17. (a) Octavius detector; **(b)** Ionization chamber

Table 3. Specification of Treatment planning system (TPS) and medical linear accelerator [106, 107]

Treatment planning system (TPS)			**Medical Linear accelerator**		
Manufacturer	Elekta	Varian	Manufacturer	Elekta	Varian
Model	Monaco	Eclipse		Infinity	Halcyon
Version	5.11.03		Serial number	-	-
Calculation algorithm	Monte Carlo	Eclipse	Installation year	2015	2021
Calculation grid size (mm)	3	3	Multi leaf collimator (MLC) model	Agility 160 leaves, 0.5 cm leaf width	Dual-layer MLC, 114 (29/ bank on proximal, 28/ bank on distal)
			Photon energy	6 MV and 15 MV	(6 MV-FFF)
			Electron energy	6, 9, 12, 15, and 18 MeV	-
			Beam delivery mode	3D, IMRT, VMAT, SBRS	3D, IMRT, VMAT

2.2. Output factor for small fields shaped with MLC

The no. of monitor unit is calculated for five different small fields multi-leaf collimator (MLC) shapes (10×10 cm^2, 6×6 cm^2, 4×4 cm^2, 3×3 cm^{2,} and 2×2 cm^2). Total 10 Gy of the dose is delivered at the depth of 10 cm with SSD (source-surface distance) at 100 cm. The tolerance level of ± 3% for 2×2 cm^2 field size and larger field size ± 2% is applied. Virtual water phantom of physical dimension $30 \times 30 \times 30$ cm^3 was created in the Monaco treatment planning system and the monitor unit was calculated at a depth of 10 cm with an SSD of 100 cm where MLC is symmetric overall filed sides at a central axis.

2.3. Small MLC shape of 2×2 cm^2 field profiles test

In-plane (at a right angle to the MLC leaf motion) and cross-plane (along with the MLC motion) profiles of MLC were evaluated based on virtual water phantom generated in Monaco treatment planning system at a depth of 10 cm and extracted as a line profile. The no. of monitor unit required to deliver 6 Gy of dose at 10 cm depth with SSD of 100 cm was calculated with the profile length not less than 5 cm from the central axis. The comparisons between field size and penumbra width (20%-80%) with measured and baseline data were evaluated. The deviation greater than ±3 mm needs additional investigation. In-plane and cross-plane profiles submitted with the following information represented in table 4.

Table 4. Table Different parameter values for MLC profile test

In-plane and cross-plane profiles to be submitted	
MLC field size	2x2 cm^2
Secondary Jaw	10x10 cm^2
Calculation resolution	1 mm
SAD	100 cm
Depth	10 cm

2.4. SHANE phantom

SHANE is an anthropomorphic phantom developed by the International atomic energy agency (IAEA) for the performance of the dosimetry audit process for head and neck cancer. SHANE is "Shoulders head and neck end to end" and is applicable for every step in the radiotherapy process from image acquisition, treatment planning, to dose verification. The physical shape of the phantom is designed based upon the complex anatomical structure of the head and neck region and made from similar density materials with soft tissue, muscles, bone, and teeth, which reflects the equivalence radiation interaction properties as a real patient. The phantom can be dissembled to insert the film. It consists of four hollow cylindrical channels so that an ionization chamber can be inserted to measure the absorbed dose in cross ponding anatomical structure. Cortical bone, trabecular bone, lung inhale, lung exhale) and vial with water is present in shoulder regions to perform the calibration curve between CT number and relative electron density. The physical shape of the SHANE phantom and its components are shown in figure (18).

(a) **(b)**

Fig.18 (a). Anthropomorphic SHANE phantom; (b). SHANE phantom components [105]

2.5. Image acquisition using Computed tomography scanning

The CT scanning of SHANE was done using Manufacturer Philips Brilliance Big Bore; kV – 120kV; slice thickness1mm. The required CT image was taken for the specification needed as per the treatment planning system to delineate the target and organs at risk. Different density inserts points in the shoulder region were filled with ceramic solid rods and water is filled for the vial supply region. Different CT images clearly define the position of the ion chamber and a 3D view of the phantom is represented in the figure (19).

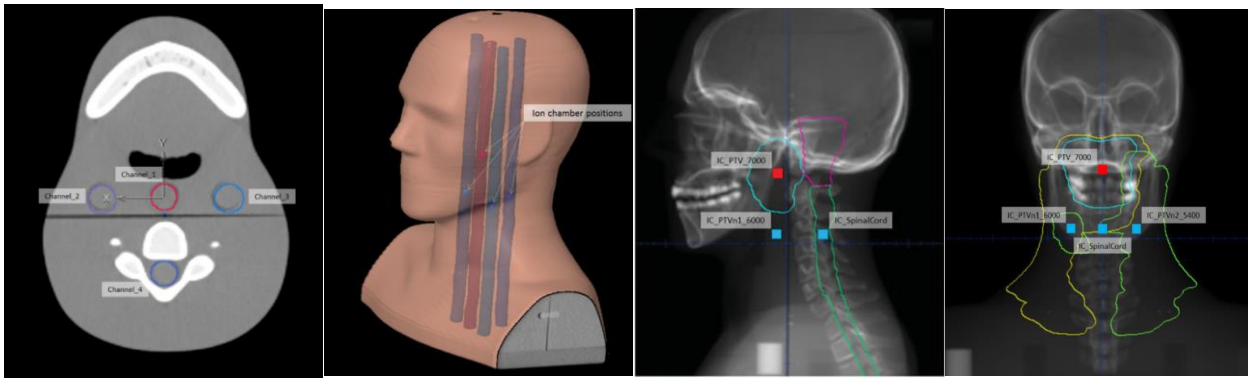

Fig. 19. CT image of H&N phantom representing the ion chamber position in a different view (transverse, 3D view, sagittal and coronal view) [105].

2.6. Relative Electron density conversion curve

To obtain a Relative Electron density conversion curve, a CT electron density phantom (Gammex) was scanned using Philips Brilliance Big Bore CT scanner with 3 mm slice thickness and 120 kV tube potential. It covers the larger variation of density materials rods corresponding to the different tissue densities. The specification of the rods follows recommended by ICRU-44 and ICRP requirements. The different densities of phantom structures are tabulated in table 5.

Table 5. Electron density for Different phantom structures.

Phantom structures	Mass density g/ cm^3	Electron density x 10^{23} /cm3	Relative electron density
Air (H)	0	0	0.000
Lung inhale (E)	0.205	0.668	0.200
Lung exhale (D)	0.5	1.648	0.493
Water (A)	1	3.34	1.000
Soft tissue (G)	1.055	3.434	1.028
Spinal cord (F)	1.07	3.488	1.044
Trabecular bone (C)	1.2	3.863	1.157
Cortical bone (B)	1.93	5.956	1.783

2.7. Volume definition

Volume definition for treatment planning includes clinical target volume (CTV), planning target volume (PTV), organs at risks, and the structure within the phantom relating to the measurement positions of the ion chamber. SHANE phantoms volume definition consists of the following structure; Planning target volume (PTV) and organs at risks; parotid _R, parotid _L, PTV_700, PTVn1_6000, and spinal cord required for treatment planning.

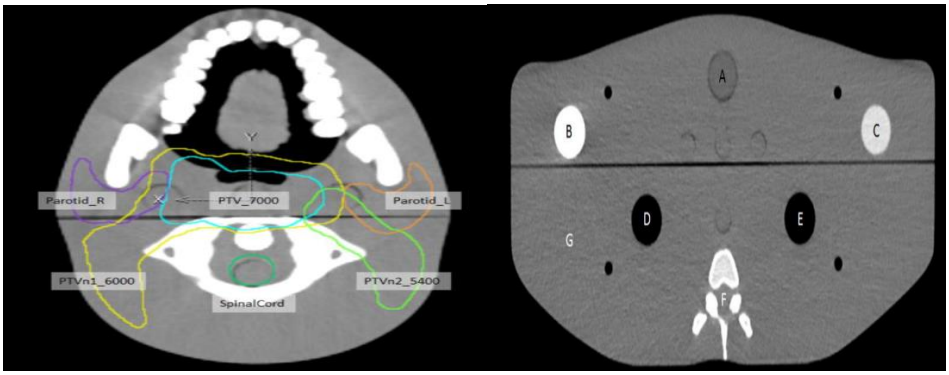

Fig. 20. CT Images of the target volume and shoulder region with different electron densities plugs organs at risk

2.8. Clinical implementation of an ionization chamber

Calibrated ion chamber model (PTW 30013-2703) with active volume 0.06 cm^3 is used for the measurement of observed dose in predefine location within the SHANE phantom. The measured dose is calculated by an electrometer connected with an ionization chamber using a fibre cable.

2.9. The treatment plan for Electra linear accelerator using Monaco TPS.

The target volume and OARs were taken from the CT image (DICOM) to the scanned H&N phantom for treatment planning. The plan was generated with the Monaco treatment planning system. Simultaneous integrated boost (SIB) schedule, three different PTVs PTV_7000, PTVn1_6000, and PTVn2_5400 with cross ponding dose as; 70 Gy, 60 Gy, and 54 Gy respectively with total 30 fractions was prescribed. For the dose towards the organs at risk; the parotid glands,

brain stem, and spinal cord the plan should be accepted with the ICRU-83 protocol. Ion chamber (IC) cavity volume contains within the PTV and spinal cord and is named as; IC_PTV_7000, IC_PTVn1_6000, IC_PTVn2_5400, and IC_Spinal Cord to measure the dose in the respective position.

The DVH value of (D98%, D50%, and D2%) and OAR are recorded. The plan was developed for the volumetric arc therapy (VMAT) technique. The plan is loaded and transfer to the machine. The Dose is delivered by VMAT full arch technique with 6 MV photon energy and total no. of monitor unit as 1052.50. The overall display of TPS and the dose-volume histogram is represented in figure (21) below.

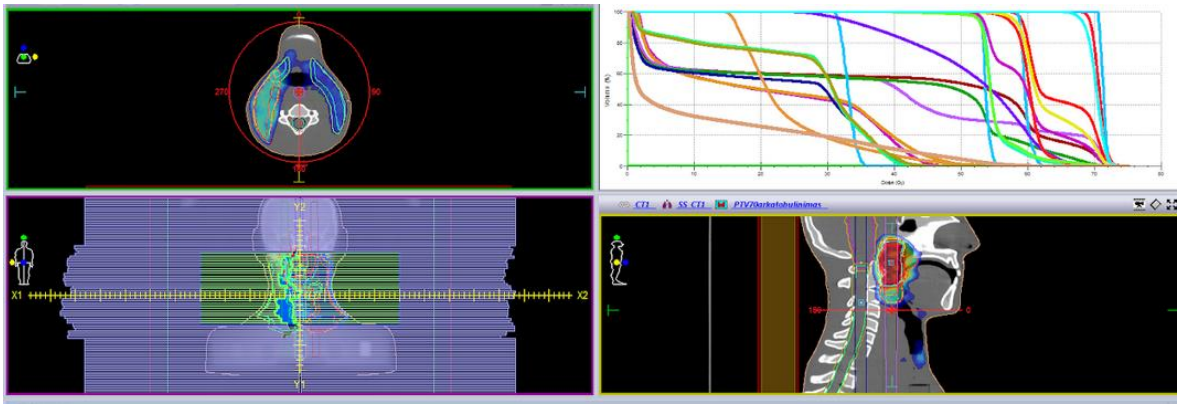

Fig. 21. Beam delivery using VMAT technique and DVH of different structure

2.10. Patient-specific Quality assurance

Patient-specific QA performed as routine work for complex dose delivery techniques such as VMAT, which used the highly modulated radiation beam and can be the reason for the discrepancy between the planed and mechanical movement of the machine. I.E. Mohamed et al [108] implements the concept of gamma evaluation for calculating the discrepancy between the planned and measured dose to detect the dose error during the irradiation. Gamma index was performed based on the selected value of distance to arrangement (DTA) and Dose difference (ΔD) and the threshold value. Global gamma referred to the 3%/3 mm with a threshold value of 10% is recommended. Gamma index less than unity is accepted.

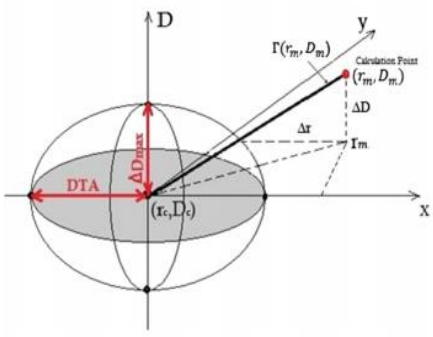

Fig.22. Concept of gamma evaluation [108]

The mathematical concept of gamma evaluation is mathematically expressed as;

$$1 = \sqrt{\frac{(\Delta r)^2}{(DTA)^2} + \frac{(\Delta D)^2}{(\Delta DMax)^2}} \quad (4)$$

$$\text{Where, } (\Delta r) = |\ r_c - r_m\ | \quad (5)$$

$$\Delta D = D_m\ (r_m) - D_c\ (r_c) \quad (6)$$

In our study, the Octavius detector system (PTW 729) as a patient-specific quality assurance was performed. It evaluates the dose distribution with a treatment planning system by reconstructing the 3D dose volume with the detector phantom. 2D ionization chamber was fitted within the detector in such a way that the centre of the array at the centre of the phantom 729-ion chamber was arranged with a spacing of 1 cm from centre- centre. The detector array is perpendicular to the beam position to avoid the angular dependence of the detector response. 3D gamma evaluation was performed with the overall 3D dose distribution comprising TPS and the reconstructed 3D measurements dose.

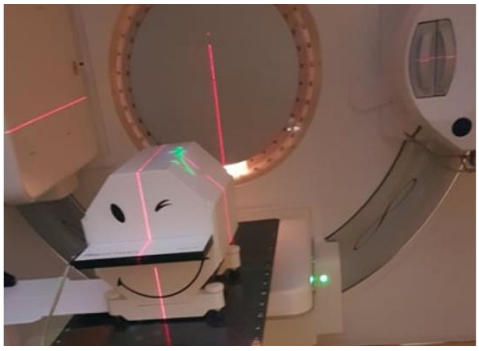

Fig. 23. Octavius 729 detector positioned on the couch

2.10. Pre-treatment imaging

To reduce the uncertainty in the positioning of the phantom, image-guided procedures are takes placed. The phantom is aligned on the treatment couch and positioning is adjusted with leaser. CBCT beam is taken using on-board imaging modalities. It generates the 180 slices CT image and gets the volumetric image to compare with the reference CT image and adjust the positioning of the phantom.

Fig.24. Pre-treatment imaging using KV CBCT imaging

2.11. Halcyon accelerator ‘O’ ring lilacs

All the measurements for Halcyon accelerator-based upon the IAEA end-to-end test audit methodology. The treatment planning was done using the recommendation given by protocols for the head and neck treatment plan. The plan generated using the Eclipse treatment planning system with SIB VMAT dose delivery. The value Dose-volume information of PTVs, organs at risks, and other structures are evaluated. The Dose is delivered with 321.6 and 336.5 no. of the monitor unit for two arc rotations. The treatment planning windows and Dose-volume histogram (DVH) is represented in fig. 25 and 26 respectively.

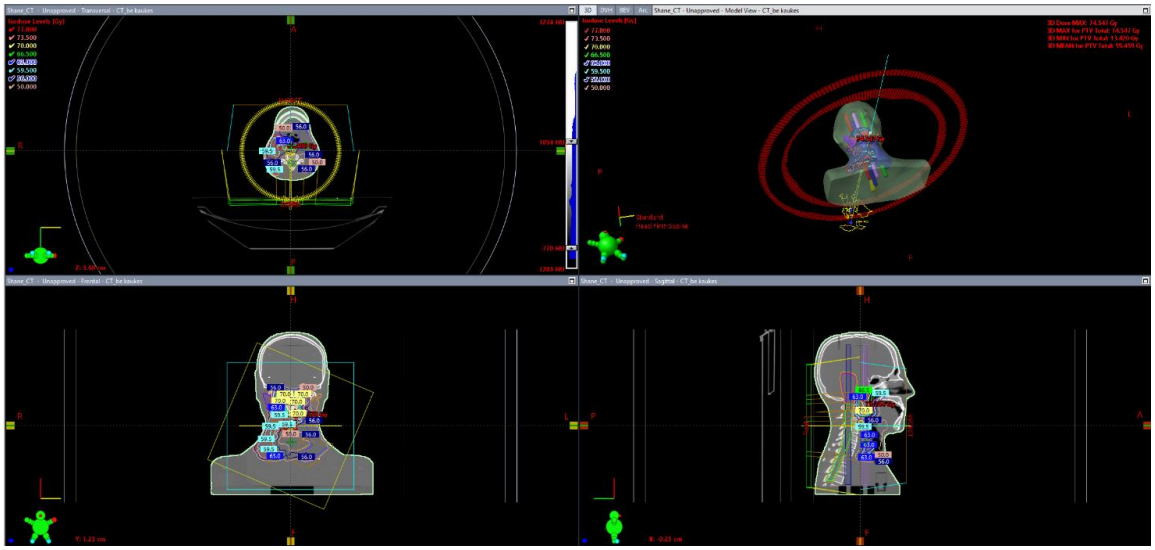

Fig. 25. TPS window of Eclipse TPS for SHANE phantom

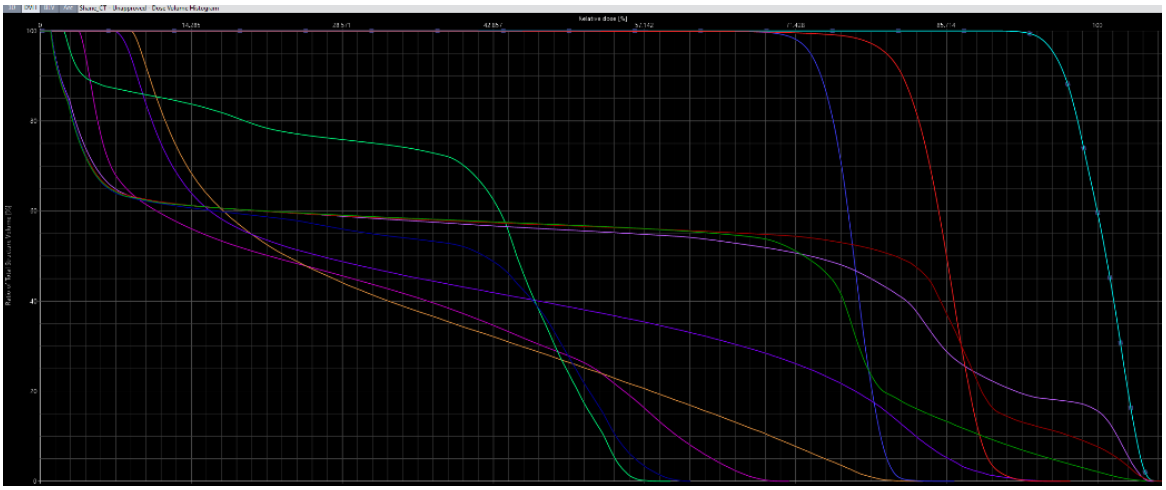

Fig. 26. Dose-volume histogram (DVH) of different structure

2.12. Calculation

2.12.1. Dose difference

The calculation of dose difference between treatment planning (TPS) calculated dose and ion chamber measured within the structure volume of the phantom is given by the equation (6) and Ion chamber measurement is recalculated using TRS-398 protocols.

$$\text{Dose Deviation (\%)} = \frac{(\boldsymbol{D_{cal} - D_{means}})}{\boldsymbol{D_{means}}} \times 100 \quad (6)$$

Where, D_{means} = dose value measured using ion chamber at respective point;

D_{cal} = calculated dose in treatment planning.

2.12.2. Homogeneity index calculation

The homogeneity index was calculated based upon the dose-volume information. The dose to the minimum, maximum, and mean dose was taken from TPS and calculated by using equation (8),

$$\text{Homogeneity index (HI)} = \frac{D_{min} - D_{max}}{D_{mean}} \quad (7)$$

Where, D_{min} = minimum dose to the given volume

D_{max} = Maximum dose to the given volume

D_{mean} = Mean dose to the given volume

3. Results and Discussion

3.1. Monitor unit calculations for different field sizes

The output factor for MLC's different field along with the sizes monitor unit is represented in the table below. The highest no of monitor units is required for the small field size of 2×2 cm^2 as 1781.46 and for the largest field size, 10×10 cm^2 was found a minimum of 1447.99.

The recommended tolerance level for small field 2×2 cm^2 is ± 3% and for larger field size is ± 2%. The deviation for all field sizes is found to within the tolerance level. The deviation values in the output factor were calculated by comparing them with the provided reference data. The maximum deviation was found to be 2.24 % for (6×6) cm^2 field size. The graphical representation of output factors vs field size shows the linear relationship illustrated by fig. 27.

Table 6. Monitor unit (MU) calculations for the MLC with different field sizes

Square field side [cm^2]	**MUs to deliver 10 Gy to prescription point**	**Output factor**	**Reference data**	**Deviation (%)**
10	1447.99	1.000	1.000	0.0
6	1579.13	0.917	0.938	2.24
4	1664.68	0.870	0.886	1.81
3	1724.82	0.840	0.851	1.29
2	1781.46	0.813	0.804	1.11

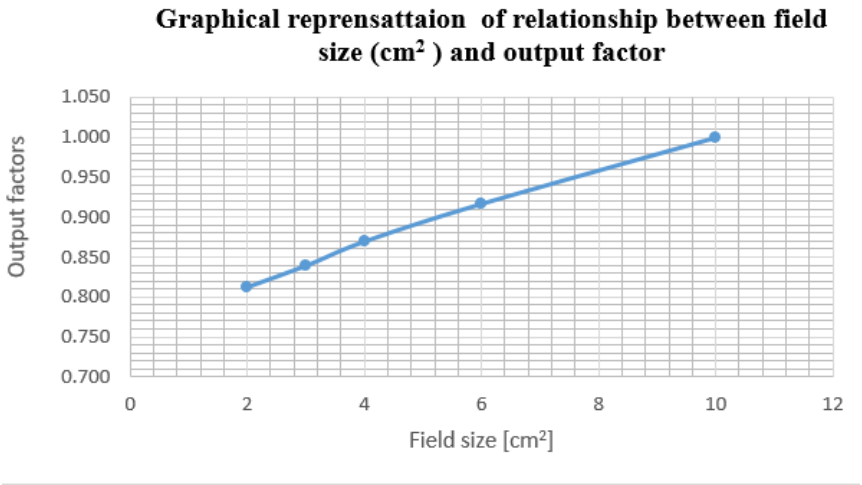

Fig. 27. Graphical representation of output factors vs field size

The linearity in output factor vs field size represents the increasing output factor with increasing field size. The relatively larger variation in field size causes significant increases in uncertainty in

output factors, especially for the small field size. For smaller field size phantom scattering is relatively small due to the sharply increases lateral electronic equilibrium. Therefore, the small field dosimetry needs very precise measurement due to the obstacle associated with lateral electronic equilibrium and selecting the appropriate detectors.

3.2. In-plane and cross-plane profile

Table 7. In-Plane and cross- Plane profile result

	In-plane	Cross- plane	Tolerance level
Right penumbra, cm	0.36	0.46	3mm
Field size, cm	2.12	2.16	2 mm
Left penumbra, cm	0.34	0.46	3mm

The graphical representation of In-plane and cross-plane profiles are shown in the figure (28 and 29).

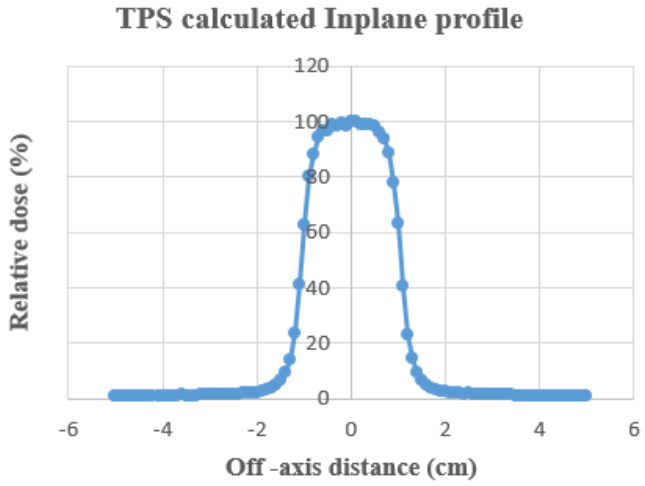

Fig. 28. In-plane profile of MLC for small field size

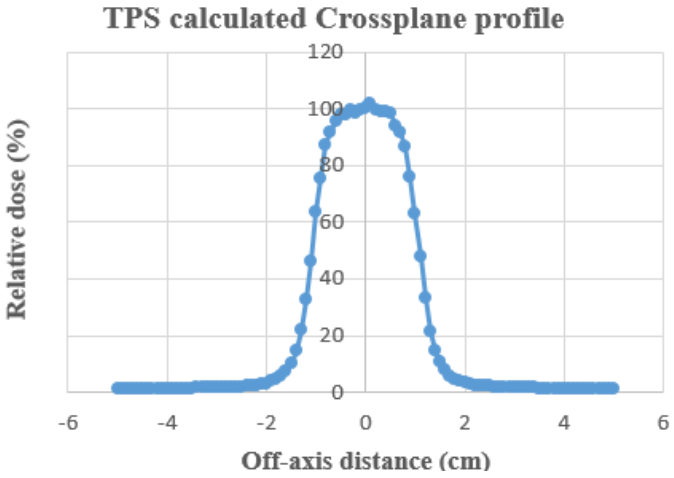

Fig. 29. Cross-plane profile of MLC for small field size

Virtual water phantom is generated in the Monaco treatment planning system and inplane and cross-plane profiles are calculated and presented in graphical form. Field size and penumbra width (20-80) % were compared with the baseline data obtained from the IAEA. The deviation within the ±3 mm is accepted. For both plane profiles, the deviation in penumbra size was within the tolerance limit of ±3 mm and not exceeded ±2 mm for field size.

3.3. CT Hounsfield unit and relative electron density conversion

The relative electron density and Hounsfield unit for measured and calculated CT are tabulated below (Table 8). The Tolerance value for water is ±5 HU and for other materials ±20 HU. The HUs of all the phantom structures are within the tolerance level as described in table 8.

Table 8. Relative electron density and Hounsfield unit conversion

	Measured CT calibrated data		**CT calibrated data from TPS**		**Difference between curves**	
Phantom structures	**Relative electron density**	**Measured CT calibration data HUs**	**Relative electron density**	**Measured CT calibration data HUs**	**Cross ponding HU in measured CT calibration data**	**The difference in HUs for curved.**
Air (H)	0.00	-1001.7	0.003	-999	-998	1
Lung inhale(E)	0.200	-761.1	0.199	-764	-762	2
Lung exhale(D)	0.493	-545	0.493	-544	-545	-1
Water(A)	1.000	-8.5	0.996	-7	-13	-6
Soft tissue(G)	1.028	18.9	1.030	17	23	6
Spinal cord(F)	1.044	58.3	1.053	60	75	15
Trabecular bone(C)	1.157	274.2	1.156	275	273	-2
Cortical bone (B)	1.783	1319.7	1.784	1318	1321	3

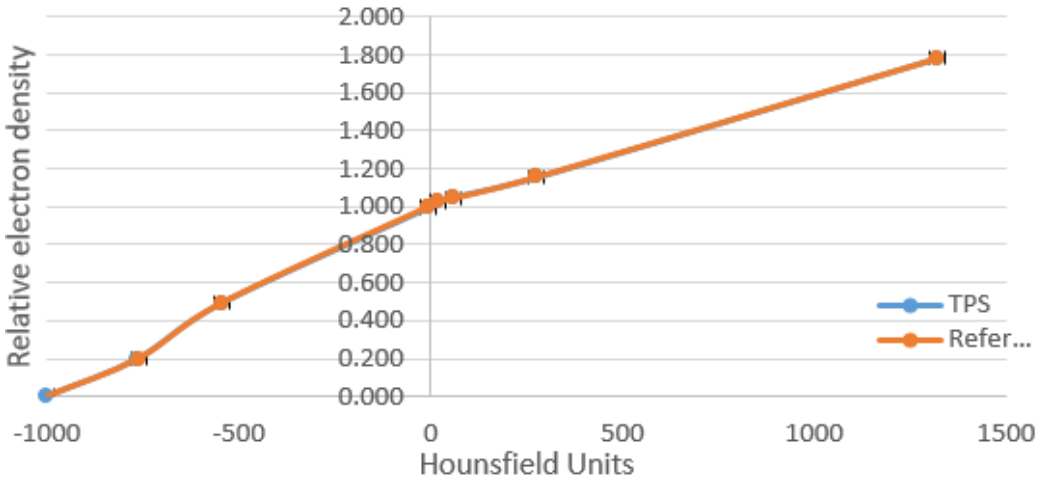

Fig. 30. Hounsfield unit vs relative electron density conversion curve

Hounsfield unit vs relative electron density conversion curve for reference and TPS shows the overlap for most of the structure with the deviation of very few units. The maximum deviation was found for the point F corresponding to the spinal cord with 16 HU and for other structures shows the minimum difference not exceeding the difference of 6 HU. For low KV photon energy, the interaction of photon materials is due to the photoelectric effect, which depends upon the atomic number. In contrast for Compton scattering relies on the electron density of the materials. The variation in larger Hounsfield units in curves is related to the materials with higher effective atomic numbers corresponds to the spinal cord. The relation between the Hounsfield unit and relative electron density was taken for heterogeneity corrections during dose calculations.

3.4. The volume of the SHANE phantom structure

The volume of the different structures within the SHANE phantom is described in table 9. These specific values of volume were provided by the CIRS manufacturing company and calculated volume from TPS. The deviation in volume for all the structures is within the tolerance level as prescribed.

Table 9. SHANE volume information for a different structure

Structure name	Description	Reference volume, cm^3	Calculated volume (cm^3)	Volume difference	Tolerance level
PTV_7000	Nasopharynx primary plan target	88.5	88.742	0.242	1
PTVn1_6000	Involved nodes plan target volume	411.6	411.508	0.092	3.5
PTVn2_5400	Elective nodes plan target volume	260.3	259.844	0.456	6
Spinal Cord	Spinal cord organ at risk	24.9	25.797	0.097	8.5
SpinalCord_03	Spinal cord Plan Risk Volume 3mm	55.1	58.465	3.365	9
Brain Stem	Brain stem organ at risk	43.9	43.886	0.014	3
BrainStem_03	Brian stem Plan Risk Volume 3mm	72.5	72.67	0.17	1.5
Parotid_L	Contralateral left parotid	19.7	19.67	0.03	4
Parotid_R	Ipsilateral right parotid	23.4	22.798	0.602	4
IC_PTV_7000	Ion chamber volume in nasopharynx	0.13	0.168	-	-
IC_PTVn1_6000	Ion chamber volume in involved nodes	0.13	0.168	-	-
IC_PTVn2_5400	Ion chamber volume in elective nodes	0.13	0.168	-	-
IC_SpinalCord	Ion chamber volume in spinal cord	0.13	0.168	-	-
Channel_1	Channel for IC_PTV_7000	42.0	47.405	-	-
Channel_2	Channel for IC_PTVn1_6000	42.0	46.938	-	-
Channel_3	Channel for IC_PTVn2_5400	42.0	47.524	-	-
Channel_4	Channel for IC_Spinal Cord	42.0	47.505	-	-

3.5. Dose distribution using gamma analysis

The patient-specific quality control result using gamma analysis represents in figure 31. 3D gamma with 3%/3 mm was evaluated with a threshold value of 20 %. The normalization was done at the point with a high dose low gradient region in the middle regions of the primary target volume (Nasopharynx).

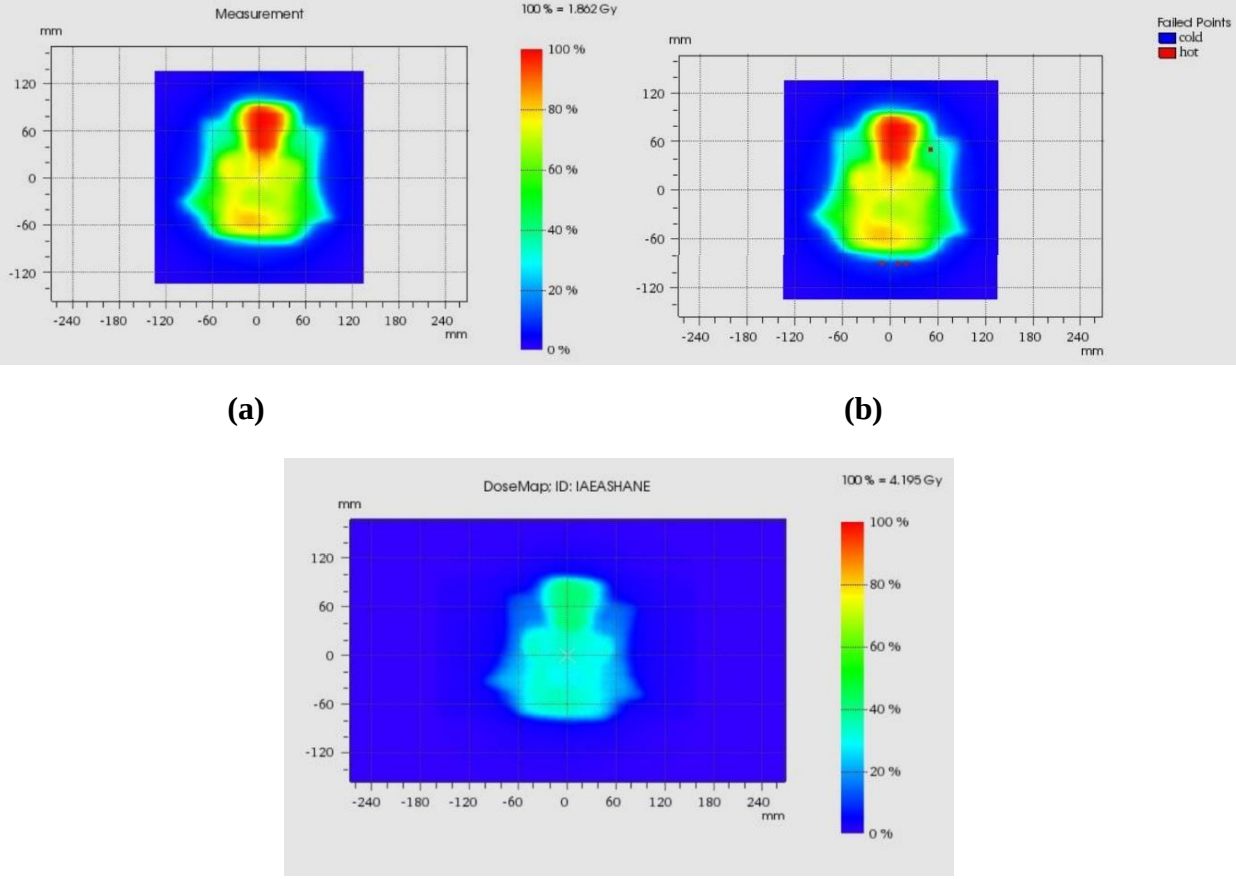

(a) **(b)**

(c)

Fig. 31. (a). Measured Dose distribution **(b)** calculated dose distribution and **(c)** dose mapping

The result of the patient-specific control using the Octavius detector shows the 98.7 % of the plan was passed and (1.3%) was failed which corresponds to the 4 points. The detector consist of 729 dose points and the evaluated dose point was 304. This represents the verification of the treatment plan with the plan threshold value of 95 % with global gamma (3%/3mm). The various studies suggest that the pons of the 2D array over film and EPID based quality assurance procedures. However, EPID and film measurement has a better spatial resolution also need an energy dependency correction factor and for the film, readout required an expensive film density scanner.

3.6. Dose-volume result of Eclipse treatment planning system

Table 10. Treatment planning result with Dose (Gy) volume information received by different phantom structures

Structure	Volume	Dose	Calculated Dose (Gy)
PTV_7000	98%	>90% (63.0 Gy)	67.163
	95%	>95% (66.5 Gy)	67.991
	50%	=100% (70.0 Gy)	70.323
	2%	<107% (74.9 Gy)	72.483
PTVn1_6000(involved nodes)	98%	>90% (54.0 Gy)	56.637
	95%	>95% (57.0 Gy)	57.917
	50%	60.0-62.0 Gy	61.144
PTVn2_5400 (elective nodes)	98%	>90% (48.6 Gy)	50.949
	95%	>95% (51.3 Gy)	52.591
	50%	54.0-56.0 Gy	54.431
Spinal Cord	2%	<45 Gy	40.534
SpinalCord_03	2%	<50 Gy	41.772
Brain Stem	2%	<50 Gy	44.768
Brain Stem _03	2%	<55 Gy	48.669
Parotid_L	Mean	<24 Gy	23.798
Parotid_R	Mean	as low as possible	51.781

The result obtained from TPS is a recommendation followed by the ICRU-83. The dose constraints for 98 %, 95 %, and 50 % volume are reported. The dosimetry aspect of treatment planning for all 9 different structures is achieved as preference given to the specific structures; Spinal cord and brain stream, and three different PTV and left and right parotid gland.

3.7. Calculated and measured dose analysis for Monaco treatment planning system

Table 11. Calculated and measured dose using ionization chamber data analysis for the Elekta infinity

Volume	Structure associated with a position of chamber	TPS calculated mean dose (Gy)	TPS calculated dose (Gy) per fraction	Homogeneity Index (HI)	Measured dose per fraction	$\frac{D_{meas}}{D_{cal}}$	The difference in a dose per fraction (%)	Tolerance level (%)
IC_PTV_7000	PTV_7000 (nasopharynx), isocentre, red channel no 1	71.36	2.38	0.03	2.33	0.98	2.14	5
IC_PTVn1_6000	PTVn1_6000 (involved nodes), 5 cm inferior to isocentre, blue channel no 2	59.74	1.99	0.07	1.96	0.98	1.53	5

Table 11. Calculated and measured dose using ionization chamber data analysis for the Elekta infinity (continued)

Volume	Structure associated with a position of chamber	TPS calculated mean dose (Gy)	TPS calculated dose (Gy) dose per fraction	Homogeneity Index (HI)	Measured dose per fraction	$\frac{D_{meas}}{D_{cal}}$	The difference in a dose per fraction (%)	Tolerance level (%)
IC_PTVn2_5400	PTVn2_5400 (elective nodes), 5 cm inferior to isocentre, blue channel no 3	53.81	1.79	0.05	1.77	0.99	1.23	5
IC_SpinalCord	IC_SpinalCord, 5 cm inferior to isocentre, blue channel no 4	33.12	1.10	0.13	1.07	0.97	2.80	**7**

3.8. Calculated and measured dose analysis for Monaco treatment planning system

Table 12. Calculated and measured dose using ionization chamber analysis for Halcyon accelerator

Volume	Structure associated with a position of chamber	TPS calculated mean dose (Gy)	TPS calculated dose (Gy) per fraction	Homogeneity index (HI)	Measured dose per fraction	$\frac{D_{meas}}{D_{cal}}$	The difference in a dose per fraction (%)	Tolerance level (%)
IC_PTV_7000	PTV_7000 (nasopharynx), isocentre, red channel no 1	72.11	2.6	0.02	2.30	0.88	-12.85	5
IC_PTVn1_6000	PTVn1_6000 (involved nodes), 5 cm inferior to isocentre, blue channel no 2	61.01	2.03	0.07	2.07	1.02	1.60	5
IC_PTVn2_5400	PTVn2_5400 (elective nodes), 5 cm inferior to isocentre, blue channel no 3	53.41	1.90	0.02	1.84	0.97	3.15	5
IC_SpinalCord	IC_SpinalCord, 5 cm inferior to isocentre,	34.091	0.92	0.19	0.94	1.02	2.57	7

	blue channel no 4							

The ionization chamber measurement for four different locations PTV_7000 (nasopharynx), isocentre, red channel no 1, PTVn1_6000 (involved nodes), 5 cm inferior to isocentre, blue channel no 2, PTVn2_5400 (elective nodes), 5 cm inferior to isocentre, blue channel no 3, IC_SpinalCord, 5 cm inferior to isocentre, blue channel no 4 for Elekta infinity (Monaco TPS) are within the tolerance level of 5 % for PTVs structure and 7 % for the spinal cord. Similarly, for the halcyon accelerator (Eclipse TPS) two PTV_IC measurements IC_PTVn1_6000, IC_PTVn2_5400, and spinal cord are 1.60 %, 3.15%, and 2.57% respectively also does not exceed the tolerance level. In contrast, for IC_ PTV 700 values are -12.85 %, which exceeds the tolerance level caused by the positioning of the active volume of the chamber is outside the radiation field. The significant difference in the region of PTVs and spinal cord reflects the need to set up for dose deviation tolerance limit. The position of the ion chamber within the phantom volume should be fitted properly for the accurate dosimetry measurement; it could be one reason for dosimetry error.

The heterogeneity of SHANE phantom shows the vital component for dosimetry measurement with the convincing result reflecting its importance in clinical practice for an overall sequence in radiotherapy. Based on this feature, a multicentre dosimetry audit was necessary to be carried out by institutions to compare the dosimetry result. The dose measurement using ion chambers and film dosimetry where would reduce the dose discrepancy and contributes to the analysis of various parameters related to the linear accelerator quality control test. The dose comparisons between the different institutions have significant importance to reduce the discrepancies that arise during irradiation and have addressed the systematic uncertainties that arise due to local discrepancies in the dosimetric methodology conducted by each institution.

The bar diagram of the dose ratio comparison between the TPS calculated dose and ion chamber measured dose is presented in figure 32.

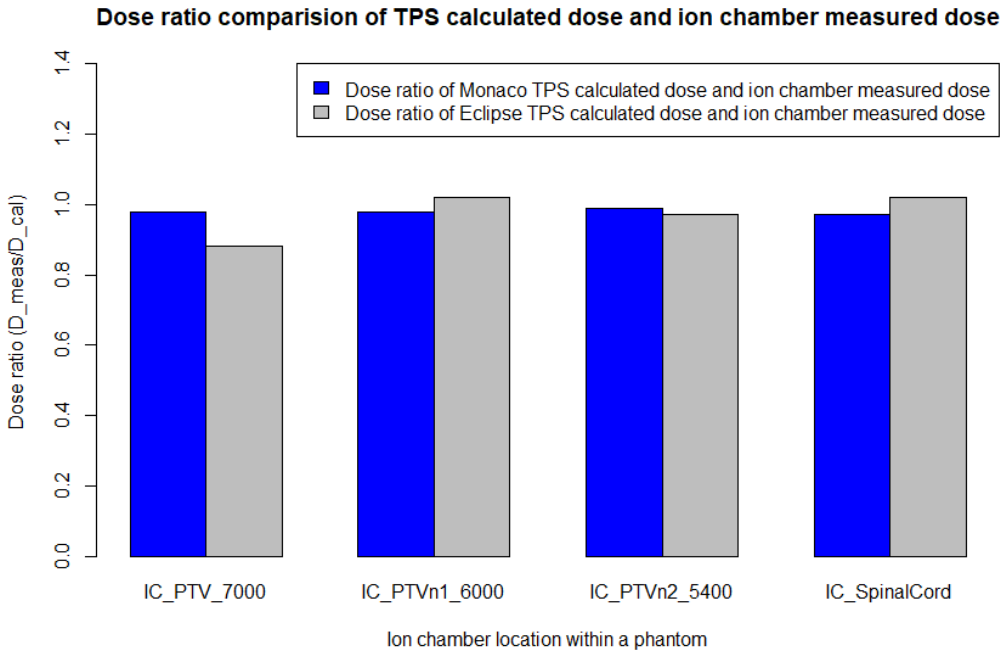

Fig.32. Comparison of dose ratio between TPS calculated dose and ion chamber measured dose

The dose ratio of the treatment planning system (Monaco and Eclipse) calculated dose and ion chamber measured dose for the primary target volume, PTV_7000 shows the dose ratio is a significant difference caused by the error that arises in the positioning error of the ion chamber within the phantom volume, and for the other two IC_PTVn1_6000, IC_PTVn2_5400 and spinal cord shows the slight difference in dose ratio. The dose ratio closed to the unity implies the minimum discrepancy between measured and calculated doses.

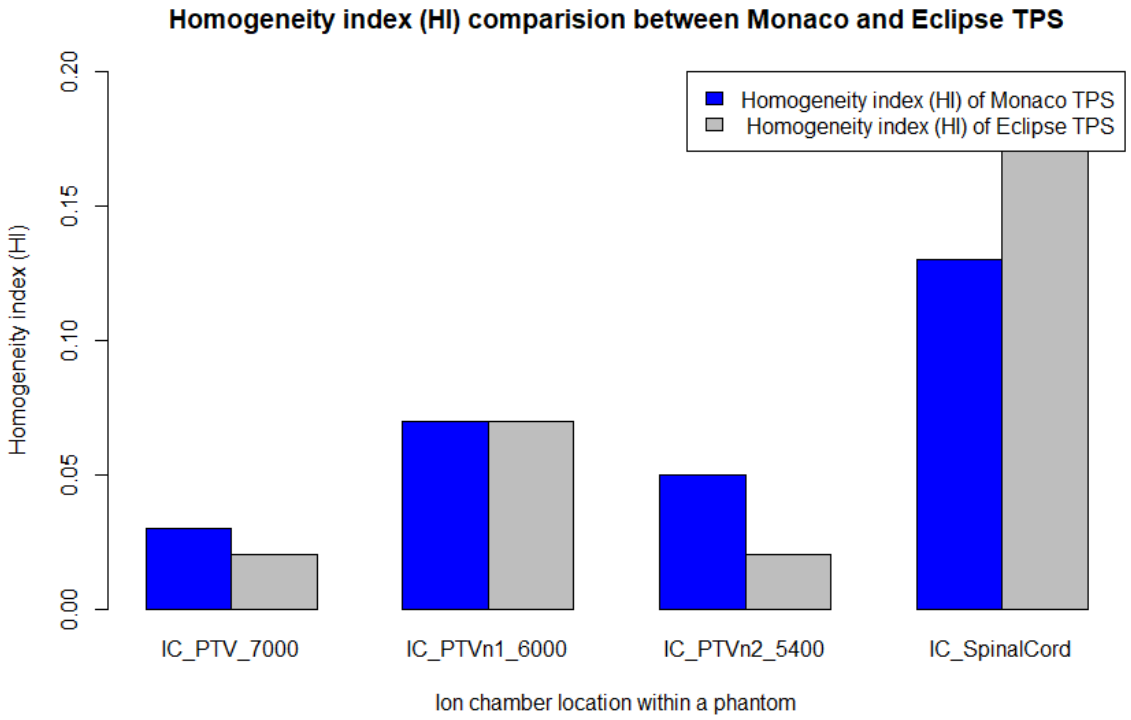

Fig.33. Homogeneity index comparison between Eclipse and Monaco TPS

The homogeneity index reflects the dose uniformity towards the target volume. The homogeneity index (HI) for PTV was between 0.02 and 0.19, where HI=0 indicates the optimum uniformity dose level within the target volume indicated by the sequences of the DVH followed by ICRU 83. The bar graph for two different plans with four regions of interest (three PTVs and spinal cord) shows the significant difference homogeneity index for PTV_7000, IC_ PTV n2_5400, and IC-spinal cord for two plans. However, for the IC_PTVn1_6000 with an equal proportion of dose uniformity.

4. Conclusions

1. The calculated value of the output factor for all five different field sizes is within the tolerance level as ±3 % as it is recommended, while for (2×2) cm^2 was within ±2 %. In-plane and cross-plane profiles for the small field size (2×2) cm^2 left and right penumbra was not exceeded the tolerance limit.

2. The CT number and a calibration curve of relative electron density showed that variation in Hounsfield unit values was within the tolerance limit for all measured points, while the largest difference was found (15 HU) for the critical organ (spinal cord) point F. This difference was influenced by the type of phantom and parameters selected in the CT unit.

3. The patient-specific quality control test, using Octavius detector showed, that plan with 98.6 % was passed with a gamma value of 3%/3 mm, normalized at the point of high dose low gradient region of the central part of PTV_7000, evaluated at a threshold of 20 % with plan acceptance criteria of 95%.

4. The dose difference between TPS calculated dose and ionization chamber measurements for three different PTVs points IC_PTV_7000 (1.81%), IC_PTVn1_6000 (1.34%), IC_PTVn2_5400 (1.06%), and IC_Spinal Cord (2.94%), were within the tolerance limit of 5% and 7% respectively for Elekta Infinity. The same tendency was observed and for linear accelerator Halcyon (IC_PTVn1_6000 (1.61%), IC_PTVn2_5400 (3.15 %), and spinal cord (2.57 %), with an exception of IC_PTV_700 (-12.85 %) point, which was out of irradiation field.

5. References

1. Hyun Do Huh, Seonghoon Kim, History of Radiation Therapy Technology. Progress in Medical Physics. 2020, Vol. 31.
2. Hugo Palmans, Pedro Andreo, M. Saiful Huq, Jan Seuntjens, Karen E. Christaki, Ahmed Meghzifene. Dosimetry of small static fields used in external photon beam radiotherapy: Summary of TRS-483, the IAEA–AAPM International Code of Practice for reference and relative dose determination. 2018, vol.45, pp. 1123-1145.
3. S. D. Sharma., Challenges of small photon field dosimetry are still challenging, J Med Phys. 2014, Vol. 39, pp.131– 132.
4. Kazantsev P, Lechner W, Gershkevitsh E, Clark CH, Venencia D, Van Dyk J, Wesolowska P, Hernandez V, Jornet N, Tomsej M, Bokulic T, Izewska J. IAEA methodology for on-site end-to-end IMRT/VMAT audits an international pilot study. Acta Oncol. 2020, Vol.59, pp.141-148.
5. Azzam Patrick, Mroueh Manal, Francis Marina, Abou Daher Alaa, Zeidan Youssef H Radiation-induced neuropathies in head and neck cancer: prevention and treatment modalities cancer. 2020, Vol. 14.
6. Francesca De Felice, Antonella Polimeni, Valentino Valentini, Orlando Brugnoletti , Andrea Cassoni, Antonio Greco, Marco de Vincentiis and Vincenzo Tombolini. Radiotherapy Controversies and Prospective in Head and Neck Cancer: A Literature-Based Critical Review. 2018, Vol. 20, pp. 227–232.
7. Daniel E. Johnson, Barbara Burtness, C. René Leemans, Vivian Wai Yan Lui, Julie E. Bauman, Jennifer R. Grandis. Head and neck squamous cell carcinoma. Nat Rev Dis Primers. 2020, vol. 6**.**
8. Liu Jie, Han Mengmeng, Yue Zhenyu, Dong Chao, Wen Pengbo, Zhao Guoping, Wu Lijun, Xia Junfeng, Bin Yannan. Prediction of Radiosensitivity in Head and Neck Squamous Cell Carcinoma Based on Multiple Omics Data. Journal of Frontiers in Genetics. 2020, Vol.11, p. 960.
9. Metin Figen, Didem C¸ Olpan Öksüz, Evrim Duman, Robin Prestwich, Karen Dyker, Kate Cardale, Satiavani Ramasamy, Patrick Murray and Mehmet S¸ Radiotherapy for Head and Neck Cancer: Evaluation of Triggered Adaptive Replanning in Routine Practice Metin Figen. 2020.
10. Waqar M, Nawaz Abro M, Soomro Q, Shaaban M, Khatoon S. Retrospective Incidence Analysis of Head and Neck Cancer Patients in Rural Areas of Sindh, Pakistan, Jundishapur J Chronic Dis Care. 2019, Vol. 8.
11. Trinanjan basu, Nithin Bhaskar. Overview of important organ at risk (OAR) in modern radiotherapy for head and neck cancer (HNC). 2018. DOI: 10.5772/intechopen.80606.
12. Paulo Martins. A brief history of radiotherapy. International Journal of Latest Research in Engineering and Technology (IJLRET). 2018, Vol. 4, pp. 08-11.
13. Hyun Do Huh, Seonghoon Kim. History of Radiation Therapy Technology.2020, vol. 31.
14. C. M. L. WEST S. E. DAVIDSON S. A. G. ELYAN R. SWINDELL S. A.ROBERTS C. J. ORTON C. A. COYLE H. VALENTINE D. P. WILKS R. D. HUNTER J. H. HENDRY. The intrinsic radiosensitivity of normal and tumor cells, International Journal of Radiation Biology. 2009, Vol. 73, pp. 409-413.

15. Thompson, M.K, Poortmans, P. Chalmers, A.J. et al. Practice-changing radiation therapy trials for the treatment of cancer: where are we 150 years after the birth of Marie Curie?. Br J Cancer. 2018, Vol. 119, pp.389–407.
16. Kaiser, A., Eley, J.G., Onyeuku, N.E., Rice, S.R., Wright, C.C., McGovern, N.E., Sank, M., Zhu, M., Vujaskovic, Z., Simone 2nd, C.B., Hussain, A. Proton Therapy Delivery and Its Clinical Application in Select Solid Tumor Malignancies. J. Vis. Exp. 2019, Vol.114, pp. 1-12.
17. Serena Gianfaldoni, Roberto Gianfaldoni , Uwe Wollina , Jacopo Lotti , Georgi Tchernev , Torello Lotti. An Overview on Radiotherapy: From Its History to Its Current Applications in Dermatology. Open Access Macedonian Journal of Medical Sciences. 2017 vol. 5, pp. 521-525.
18. Supriya Mallick, Rony Benson, Pramod K. Julka, Goura K. Rath. Review altered fractionation radiotherapy in head and neck squamous cell carcinoma. Journal of the Egyptian National Cancer Institute. 2016, vol. 28, pp. 73-80.
19. Kean F. Ho, Jack F. Fowler, Andrew J. Sykes, Beng K. Yap, Lip W. Lee & Nick J. Slevin IMRT dose fractionation for head and neck cancer: Variation in current approaches will make standardization difficult, Acta Oncologica. 2009, vol. 48, pp.431-439.
20. Adachi, W, Hehr, T. Budach, V. et al. A meta-analysis of hyper fractionated and accelerated radiotherapy and combined chemotherapy and radiotherapy regimens in unresected locally advanced squamous cell carcinoma of the head and neck. BMC Cancer. 2006, Vol. 28.
21. Matuschek, C., Haussmann, J. Bölke, E. et al. Accelerated vs. conventionally fractionated adjuvant radiotherapy in high-risk head and neck cancer: a meta-analysis. Radiat Oncol, 2018 Vo. 13**.**
22. Charles M Able, Carnell J Hampton, Alan H Baydush, and Michael T Munle. Initial investigation using statistical process control for quality control of accelerator beam steering. Radiation Oncology. 2011, Vol.6.
23. Technical specifications of radiotherapy equipment for cancer treatment. Geneva: World Health Organization; 2021. License: CC BY-NC-SA 3.0 IGO.
24. Koren Smith, Peter Balter, John Duhon, Gerald A. White Jr, David L. Vassy Jr, Robin A. Miller, Christopher F. Serago, Lynne A. Fairobent. AAPM Medical Physics Practice Guideline 8.a.: Linear accelerator performance tests. 2017, Vol.18, pp. 23-39.
25. BAGNE, F. Physical aspects of super voltage x-ray therapy. In Medical Physics [interactive]. 1974, Vol. 1, pp. 266–274.
26. International Atomic Energy Agency, Dosimetry and Medical Radiation Physics Section, Applied Radiation Biology and Radiotherapy Section, Vienna (Austria). The transition from 2-D radiotherapy to 3-D conformal and intensity-modulated radiotherapy (IAEA-TECDOC--1588). International Atomic Energy Agency (IAEA), 2008.
27. Julie van der Veen ID and Sandra Nuyts .Can Intensity-Modulated-Radiotherapy Reduce Toxicity in Head and Neck Squamous Cell Carcinoma? 2017, Vol. 9.
28. Hanan A. Abotaleb, Ehab Maarouf, F. M. El-Hossary, M. Raif, and Mohamed Kelany. Conformity and Homogeneity Indices for Head and Neck Cancer Patients using 3DCRT. Sohag Journal of Science. 2017, pp 1-7.

29. Mohamed Yassine Herrassi, Farida Bentayeb, Maria Rosa Malisan. Comparative study of four advanced 3d-conformal radiation therapy treatment planning techniques for head and neck cancer. Journal of medical physics. 2013, Vol. 38, pp. 98-105.
30. Dandan Xu, MM, Guowen Li, MD , Hongfei Li, MM, Fei Jia, MM. Comparison of IMRT versus 3D-CRT in the treatment of esophagus cancer. A systematic review and meta-analysis. 2017, vol. 96.
31. Sherif A AbdElWahab, Doaa A Mohammed, Ahmed M Gaballah, Mahmoud M Abdallah. Three-Dimensional Conformal versus Intensity Modulated Radiation Therapy in Treatment of Nasopharyngeal Carcinoma. The Egyptian Journal of Hospital Medicine. 2018, Vol. 71, pp. 3492-3499.
32. Amrit Kaur Mann, Indira AP, Maria Priscilla David. Recent advances in radiotherapy for head and neck cancer: a comprehensive review. International Journal of Contemporary Medical Research. 2017, Vol. 4, pp. 927-932.
33. Tejpal Gupta, Shwetabh Sinha, Sarbani Ghosh-Laskar, Ashwini Budrukkar, Naveen Mummudi, Monali Swain, Reena Phurailatpam, Kumar Prabhash, and Jai Prakash Agarwal, Intensity-modulated radiation therapy versus three-dimensional conformal radiotherapy in head and neck squamous cell carcinoma: long-term and mature outcomes of a prospective randomized trial. Radiation oncology. 2020, Vol.15, pp. 2015-2018.
34. Craig Elith, Shane E. Dempsey, DApSci, Naomi Findlay, Helen M. Warren-Forward. An Introduction to the Intensity-modulated Radiation Therapy (IMRT) Techniques, Tom therapy, and VMAT. 2011, Vol.42, pp. 37-43.
35. Doaa M. AL Zayat, Ehab M. Attalla, H.S.Abouelenein, Shady.Fadel, Wafaa Khalil, Dosimetric Comparison of Intensity-Modulated Radiotherapy versus 3D Conformal Radiotherapy in Patients with Head and Neck Cancer. Journal of Multidisciplinary Engineering Science and Technology. 2015, Vol. 2.
36. XiaoShen Wang and Avraham Eisbruch, IMRT for head and neck cancer: reducing xerostomia and dysphagia. Journal of Radiation Research. 2016, Vol. 57, pp. 69–75.
37. Tejpal Gupta1, Shwetabh Sinha, Sarbani Ghosh-Laskar, Ashwini Budrukkar, Naveen Mummudi, Monali Swain, Reena Phurailatpam, Kumar Prabhash, and Jai Prakash Agarwal. Intensity-modulated radiation therapy versus three-dimensional conformal radiotherapy in head and neck squamous cell carcinoma: long-term and mature outcomes of a prospective randomized trial. Radiation oncology. 2020, Vol.15, pp. 215-218.
38. Wong, J. “Intensity-modulated radiotherapy: current status and issues of interest Intensity Modulated Radiation Therapy Collaborative Working Group table of contents abstract introduction IMRT historical review 3D treatment planning systems Precursors to IMRT delivery systems IMRT delivery technique Scanned.” 2001, Vol.51, pp. 880-914.
39. Gabriella Macchia, Francesco Deodato, Savino Cilla, Silvia Cammelli, Alessandra Guido, Martina Ferioli, Giambattista Siepe, Vincenzo Valentini, Alessio Giuseppe Morganti3, Gabriella Ferrandina. Volumetric modulated arc therapy for treatment of solid tumors: current insights. OncoTargets and Therapy. 2017, Vol.10, pp. 3755 -3772.
40. Melissa Ghafarian, Michael Price, Manuel Morales-Paliza. Comparison of pretreatment VMAT quality assurance with the integral quality monitor (IQM) and electronic portal imaging device (EPID). 2021, Vol. 22, pp.166-175.
41. Sanjib Gayen, Sri Harsha Kombathula, Sumanta Manna, Sonal Varshney, Puneet Pareek, Dosimetric comparison of coplanar and non-coplanar volumetric-modulated arc therapy in

head and neck cancer treated with radiotherapy, radiation oncology journal. 2020, Vol. 38, pp.137-147.

42. M teoh, Ch. Clark, K wood, S Whitaker, A nisbet. Volumetric modulated arc therapy: a review of current literature and clinical use in practice. The British Journal of Radiology. 2011, Vol. 84, pp. 967–996.
43. Annamaria Didonaa, Valentina Lancellottab, Claudio Zucchetti c , Bianca Moira Panizzad, Alessandro Frattegiani , Martina Iaccoc , Anna Concetta Di Pilatoc , Simonetta Saldi , Cynthia Aristei. Is volumetric modulated arc therapy with constant dose rate a valid option in radiation therapy for head and neck cancer patients? Reports of Practical Oncology and Radiotherapy. 2018, Vol. 23, pp.175-182.
44. Gabriella Macchia Francesco Deodato Savino Cilla2 Silvia Cammelli3 Alessandra Guido Martina Ferioli3 Giambattista Siepe Vincenzo Valentini Alessio Giuseppe Morganti3, Gabriella Fernandina. Volumetric modulated arc therapy for treatment of solid tumors: current insights. OncoTargets and Therapy. 2017, Vol.10, pp. 3755–3772.
45. Steven Michiels , Kenneth Poels , Wouter Crijns , Laurence Delombaerde ,Robin De Roover , Bianca Vanstraelen , Karin Haustermans, Sandra Nuyts ,Tom Depuydt. Volumetric modulated arc therapy of head-and-neck cancer on a fast-rotating O-ring linac: Plan quality and delivery time comparison with a C-arm linac. Radiotherapy and Oncology. 2018.
46. Sanjib Gayen, Sri Harsha Kombathula, Sumanta Manna, Sonal Varshney, Puneet Pareek. Dosimetric comparison of coplanar and non-coplanar volumetric-modulated arc therapy in head and neck cancer treated with radiotherapy, Radiation Oncology Journal. 2020, Vol.38, pp. 138-147.
47. Arjunan Manikandan, Biplab Sarkar, Maitreyee Nandy, Chandra Sekaran Sureka,Michael S. Gossman, Nadendla Sujatha, Vivek Thirupathur Rajendran. Detector system dose verification comparisons for arc therapy: couch vs. gantry mount. Journal of applied clinical medical physics.2014, Vol.15.
48. Introduction of image-guided radiotherapy into clinical practice. IAEA human health report, no.16, Vienna, ISSN 2074–7667, 2019.
49. Schwarz, M., Giske, K., Stoll, A. et al. IGRT versus non-IGRT for postoperative head-and-neck IMRT patients: Dosimetric consequences arising from a PTV margin reduction. Radiat Oncol, 2012, Vol.7.
50. T. Gupta and C. Anand Narayan. Image-guided radiation therapy: Physician's perspectives. Journal of Medical Physics / Association of Medical Physicists of India. 2012, Vol.37, pp. 174-182.
51. George T. Y. Chen Æ Gregory C. Sharp Æ Shinichiro Mori, A review of image-guided radiotherapy, Radiological Physics, and Technology. 2009, Vol. 2, pp. 1–12.
52. Oupa Steven Motshweneng, Developments in radiation therapy: image-guided radiation therapy. The South African radiographer. 2019, Vol. 57.
53. Omar Abdel-Rahman, Image-Guided Radiation therapy; Basic Concepts and Clinical Potentials, Journal of Nuclear Medicine & Radiation Therapy, 2014, 5:3. DOI: 10.4172/2155-9619.1000181.
54. Shikha Goyal and Tejinder Kataria. Image Guidance in Radiation Therapy: Techniques and Applications. Radiology Research and Practice. 2014, pp. 10.

55. Maeve Kearney, Mary Coffey, Aidan Leong. A review of Image-Guided Radiation Therapy in head and neck cancer from 2009–2019 – Best Practice Recommendations for RTTs in the Clinic, Technical Innovations & Patient Support in Radiation Oncology. 2020, Vol. 14, pp. 43-50.
56. Tomas Kron, Joerg Lehmann and Peter B Greer. Dosimetry of ionizing radiation in modern radiation oncology. Physics in Medicine & Biology. 2016, Vol. 61.
57. Almond PR, Biggs PJ, Coursey BM, Hanson WF, Huq MS, Nath R, Rogers DW. AAPM's TG-51 protocol for clinical reference dosimetry of high-energy photon and electron beams. Med Phys. 1999, Vol. 26, pp.1847-70.
58. ICRP Statement on Tissue Reactions / Early and Late Effects of Radiation in Normal Tissues and Organs – Threshold Doses for Tissue Reactions in a Radiation Protection Context. ICRP Publication 118.Ann. ICRP 41(1/2), 2012.
59. GENG Chang-Ran, TANG Xiao Bin, HOU Xiao, SHU DiYun & CHEN Da, Development of Chinese hybrid radiation adult phantoms and their application to external dosimetry. Sci China Tech Sci. 2014, Vol. 57, pp. 713–719.
60. R.Polanek Z.Varga E.Fodor Sz.Brunner E.R.Szabó T.Tőkés K.Hideghéty. Improved FBX chemical dosimeter system with enhanced radiochemical yield for reference dosimetry in radiobiology and radiotherapy research. 2020, Vol.174.
61. Melissa Ghafarian, Michael Price, Manuel Morales-Paliza. Comparison of pretreatment VMAT quality assurance with the integral quality monitor (IQM) and electronic portal imaging device (EPID). Journal of applied clinical medical physics. Vol.22, pp.166-175.
62. Rita Singh, Durgeshwer Singh, Antaryami Singh. Radiation sterilization of tissue allografts: A review, World J Radiol. 2016, Vol. 8, pp. 355-369.
63. Absorbed dose determination in external beam radiotherapy: An international code of practice for dosimetry based on standards of absorbed dose verification to water, IAEA, 2000.
64. Azam Niroomand-Rad Sou-Tung Chiu-Tsao Michael P. Grams David F. Lewis Christophe G. Soares Leo J. Van Battum Indra J. Das Samuel Trichter Michael W. Kissick Guerda Massillon-JL Paola E. Alvarez Maria F. Chan, Report of AAPM Task Group 235 Radio chromic Film Dosimetry: An Update to TG-55. 2020, Vol 47, pp.5986-6025.
65. Frédéric Girard, Hugo Bouchard, Frédéric Lacroixa. Reference dosimetry using radio chromic film. Journal of applied clinical medical physics, 2012, Vol. 13.
66. Tania Santosa, Tiago Venturab, Maria do Carmo Lopes. A review on radio chromic film dosimetry for dose verification in high-energy photon beams. Radiation physics and chemistry. 2021, Vol. 179.
67. Patrizio Vaianoa , Marco Consalesa , Pierluigi Casolarob, Luigi Campajolab , Francesco Fiengac , Francesco Di Capuab, Giovanni Bregliod , Salvatore Buontempoc , Antonello Cutoloa , Andrea Cusano. A novel method for EBT3 Gafchromic films read-out at high dose levels. Physica medica. 2019, Vol. 28, pp.77-84.
68. Tania Santos TiagoVenturaMaria do CarmoLopes. A review on radio chromic film dosimetry for dose verification in high energy photon beams, Radiation Physics and Chemistry. 2020, Vol. 179.
69. Azam Niroomand-Rad, Sou-Tung Chiu-Tsao, Michael P. Grams, David F. Lewis, Christopher G. Soares Leo J. Van Battum, Indra J. Das, Samuel Trichter, Michael W. Kissick, Guerda Massillon-JL, Paola E. Alvarez, Maria F. Chan. Report of AAPM Task Group 235 Radio

chromic Film Dosimetry: An Update to TG-55.international journal of research and practice. 2020, Vol. 12, pp. 5986-6025.

70. Casolaro, P. Radio chromic Films for the Two-Dimensional Dose Distribution Assessment. Journal of Applied. Science. 2021, Vol.11, 2132. https://doi.org/10.3390/app11052132.
71. Devic S. radio chromic film dosimetry: past, present, and future. Phys Med. 2011, Vol. 27, pp 122-34.
72. Stephen F. Krya), and Paola Alvarez, Joanna E. Cygler, Larry A. DeWerd, Rebecca M. Howell, Sanford Meeks, Jennifer O'Daniel, Chester Reft, Gabriel Sawakuchi, Eduardo G. Yukihara, Dimitris Mihailidis, AAPM TG 191: Clinical use of luminescent dosimeters: TLDs and OSLDs, Med. Phys. 2020, Vol. 47.
73. Minsik Lee, Seonyeong Noh, KyoungJun Yoon, Sang-Wook Lee, Sang Min Yoon, Jinhong Jung, Chiyoung Jeong, Jungwon Kwak, Feasibility Study of Polymer Gel Dosimetry Using a 3D Printed Phantom for Liver Cancer Radiotherapy, Journal of the Korean Physical Society. 2020, Vol. 76, No. 6, pp. 453-457.
74. Baldock, Y De Deene, S Doran, G Ibbott, a Jirasek, M Lepage, K B McAuley, M Oldham, and L J Schreiner. Topical Review: Polymer gel dosimetry. Phys Med Biol. 2010, Vol. 55.
75. K B McAuley and A T Nasr, Journal of Physics: Conference Series 444 01200.1, 2013.
76. Clive Baldock Ph.D., Christian P. Karger Ph.D., Habib Zaidi Ph.D., Gel dosimetry provides the optimal end-to-end quality assurance dosimetry for MR-linacs. International journal of medical physics research and practice. 2020, Vol. 47, pp. 3259-3262.
77. Conor K McGarry, Tissue mimicking materials for imaging and therapy phantoms: review, Physics in Medicine & Biology. 2020, Vol. 65.
78. Choonsik Lee, Choonik Lee, Daniel Lodwick and Wesley E. Bolch, Nurbs- based 3-D anthropomorphic computational phantoms for radiation dosimetry applications. Radiation Protection Dosimetry. 2007, Vol. 127, pp. 227–232.
79. Almond PR, Biggs PJ, Coursey BM, Hanson WF, Huq MS, Nath R, et al. AAPM's TG-51 protocol for clinical reference dosimetry of high-energy photon and electron beams. Med Phys 1999, vol.26, pp.1847–70.
80. Faiz M. Khan, Kenneth R. Hogstrom, Ellen D. Yorke, Dimitris N. Mihailidis, M. Saiful Huq, Patrick D. Higgins, Michael G. Herman, David S. Followill, F. Christopher Deibe, John A. Antolak, Bruce J. Gerbi. Recommendations for clinical electron beam dosimetry: Supplement to the recommendations of Task Group 25. Med. Phys. 2009, Vol. 36.
81. https://www.elsesolutions.com/en/prodotti/radioterapia/physics/dosimetria-relativa/fantocci-ad-acqua-blue-phantom.
82. D. R. White, J. Booz, R. V. Griffith, J. J. Spokas, I. J. Wilson. Report 44 Journal of the International Commission on Radiation Units and Measurements. 2016, Vol. 23.
83. Matuschek, C., Haussmann, J. Bölke, E. et al. Accelerated vs. conventionally fractionated adjuvant radiotherapy in high-risk head and neck cancer: a meta-analysis. Radiat Oncol, 2018, Vol. 13**.**
84. FujioAraki. Dosimetric properties of a Solid Water High Equivalency (SW557) phantom for megavoltage photon beams. 2017, Vol. 39, pp.132-136.
85. https://www.iba-dosimetry.com/fileadmin/user_upload/rt-br-e-phantoms-for-ad_rev2_0813.pdf
86. ICRU publication 145 adult's mesh-type reference computational phantom.2019.

87. Susie Medeiros Oliveira Ramos, Sylvia Thomas, Mirta Bárbara Torres Berdeguez, Lidia Vasconcellos de Sá, Sergio Augusto Lopes de Souza, Anthropomorphic phantoms-potential for more studies and training in radiology. 2017, Vol. 2.
88. Hadi Hasanzadeh, Ali Abdullahi, Introducing a simple tissue-equivalent anthropomorphic phantom for radiation dosimetry in diagnostic radiology and radiotherapy, Journal of Paramedical Sciences. 2011, Vol.2.
89. Nina Petoussi-Henss, Janine Becker, Matthias Greiter, Helmut Schlattl, Maria Zankl, Christoph Hoeschen, Construction of anthropomorphic hybrid, dual-lattice voxel models for optimizing image quality and dose in radiography, Physics of Medical Imaging, 2014, Vol. 9.
90. Choonsik Lee, Choonik Lee, Daniel Lodwick and Wesley E. Bolch, Nurbs- based 3-D anthropomorphic computational phantoms for radiation dosimetry applications. Radiation Protection Dosimetry. 2007, Vol. 127, pp. 227–232.
91. Nina Petoussi-Henss, Wesley E Bolch, Keith F Eckerman, Akira Endo, Nolan Hertel, John Hunt, Hans G Menzel, Maurizio Pelliccioni, Helmut Schlattl and Maria Zankl. ICRP Publication 116—the first ICRP/ICRU application of the male and female adult reference computational phantoms. 2014, Vol.59.
92. Colin Paulbeck, Keith Griffin, Choonsik Lee, Harry Cullings, Stephen D. Egbert, Sachiyo Funamoto, Tatsuhiko Sato, Akira Endo, Nolan Hertel, and Wesley E. Bolch "Dosimetric Impact of a New Computational Voxel Phantom Series for the Japanese Atomic Bomb Survivors: Pregnant Females," Radiation Research. 2019, Vol.192, pp.538-561.
93. Ahmad Rafiq Mohammad Abu Arrah, Arif Faisal, Dwi Cahyani Ratna Sari, An Easily Made, Low-Cost, Bone Equivalent Material Used in Phantom Construction of Computed Tomography, International Journal of Applied Engineering Research. 2018, Vol. 13, pp. 7604-7609.
94. http://www.radimagehealthcare.com/anthropomorphic-phantoms.htm
95. Kadoya N, Abe K, Nemoto H, Sato K, Ieko Y, Ito K, Dobashi S, Takeda K, Jingu K. Evaluation of a 3D-printed heterogeneous anthropomorphic head and neck phantom for patient-specific quality assurance in intensity-modulated radiation therapy. Radiol Phys Technol. 2019, Vol.12**,** pp**.**351–356.
96. Melanie grehn, maik stille, Christian zemann, florian cremers, dirk rades and Thorsten m.buzug. A New Phantom for Individual Verification of the Dose Distribution in Precision Radiotherapy for Head-and-Neck Cancer. Anti-cancer research. 2019, Vol. 39, pp.6931-6938
97. A. Steinmann P. Alvarez H. Lee L. Court R. Stafford G. Sawakuchi Z. Wen C. D. Fuller D. Followill. MRIgRT head and neck anthropomorphic QA phantom: Design, development, reproducibility, and feasibility study. 2020, Vol. 47, pp.604-613.
98. Bao J, Chen L, Zhu J, Fei Z, Hu Z, Wang H et al . Comprehensive end-to-end test for intensity-modulated radiation therapy for nasopharyngeal carcinoma using an anthropomorphic phantom and EBT3 film. Int J Radiat Res. 2021, Vol.19 pp. 31-39.
99. Abbasi S, Khosravi M, Mehdizadeh AR, Ostovari M. A Novel Adjustable Anthropomorphic Head Phantom for Verifying the Dose of Radiation Therapy. J Biomed Phys Eng. 2020, Vol.10, pp. 663-668.
100. Izewska J, Hultqvist M, Bera P. Analysis of uncertainties in the IAEA/WHO TLD postal dose audit system. Radiation measurements. 2008, Vol. 43, pp. 959-63.

101. Izewska J, Bera P, Vatnitsky S. IAEA/WHO TLD postal dose audit service and high precision measurements for radiotherapy level dosimetry. International Atomic Energy Agency/World Health Organization. Radiation protection dosimetry. 2002, Vol. 101, pp.387-92.
102. Izewska J, Georg D, Bera P, Thwaites D, Arib M, Saravi M, et al. A methodology for TLD postal dosimetry audit of high-energy radiotherapy photon beams in non-reference conditions. Radiotherapy and oncology: journal of the European Society for Therapeutic Radiology and Oncology. 2007, Vol. 84, pp. 67-74.
103. Izewska J, Bera P, Azangwe G, Thwaites D, Georg D, Followill DS, editors. IAEA support to national TLD audit networks for radiotherapy dosimetry. . Standards, Applications, and Quality Assurance in Medical Radiation Dosimetry (IDOS): Proceedings of an International Symposium, Vienna, Austria: IAEA, 2010.
104. Paulina Wesolowska, Dietmar Georg, Wolfgang Lechner, Pavel Kazantsev, Tomislav Bokulic, Asa Carlsson Tedgren, Emelie Adolfsson, Anna Maria Campos, Victor GabrielLeandro Alves, Luo Suming, Wu-Hao, Daniela Ekendahl, Irena Konia ova, Wojciech Bulski, Krzysztof Chelminski, José Luis Alonso Samper, Sumanth Panyam Vinatha, Sougata Rakshit, Srimanoroth Siri, Milan Tomsejm, Mikko Tenhunen, Julie Povall, Stephen F. Kry, David S. Followill, David I. Thwaites & Joanna Izewska: Testing the methodology for a Dosimetric end-to-end audit of IMRT/VMAT: results of IAEA multicenter and national studies, Acta Oncologica. 2019.
105. Consultants: Catharine Clark, Eduard Gershkevitsh, Wolfgang Lechner, Jake Van Dyk, Daniel Venencia, IAEA Supported National “End-to-End” Audit Programme for Dose Delivery Using Intensity-Modulated Radiation Therapy through On-Site Visits to Radiation Therapy Institutions. 2019.
106. J Park, Q Xu, J Xue, Y Zhai, L An, Y Che. SU-E-T-119: Dosimetric and Mechanical Characteristics of Elekta Infinity LINAC with Agility MLC. International journal of medical physics research and practice, 2014, Vol.41, pp. 249-249.
107. Tze Yee Lim, Irena Dragojević, David Hoffman, Everardo Flores-Martinez, Gwe-Ya Kim. Characterization of the Halcyon^{TM} multileaf collimator system. Journal of applied clinical medical physics. 2019, Vol.20, pp.106-114.
108. Ismail E. Mohamed, Ayman G. Ibrahim, Hamdy M. Zidane, Hesham S. El-Bahkiryd,e, Adel Y. El-sahragti. Physical dosimetry of volumetric modulated arc therapy (VMAT) using EPID and 2D array for quality assurance. The Egyptian Journal of Radiology and Nuclear Medicine. 2018, Vol. 49, pp. 477- 484.

Appendices

Appendix.1. Multi-Leaf collimator profiles

For Varian accelerators, the secondary jaws are kept fixed at a 10 ×10 cm^2 field size for all MLC-defined field sizes. Make sure that the closed leaves are parked outside the field, not at the midline.

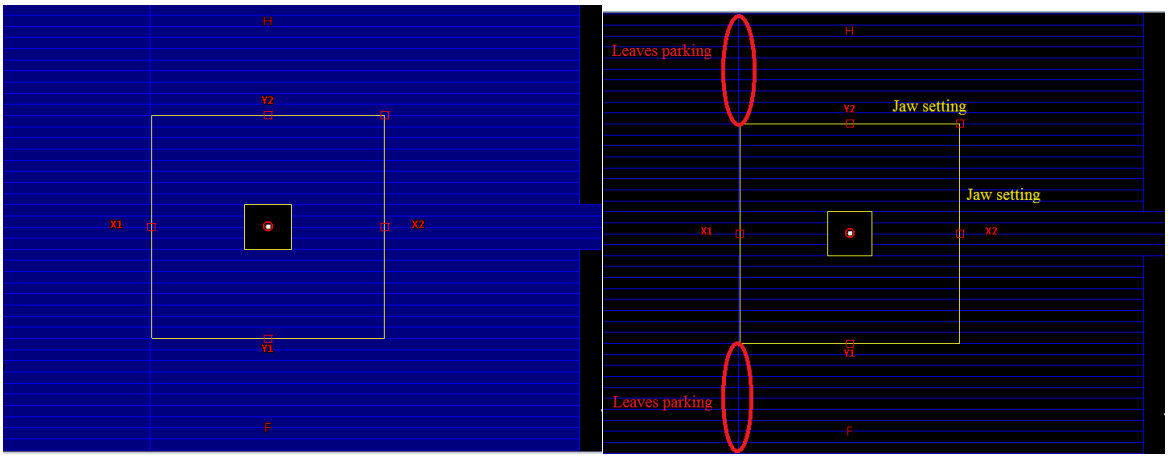

For Elekta accelerators (Agility, MLCi2) the fields are defined by MLC. 1 cm of guard leaves (2 leaf pairs for Agility, 1 leaf pair for MLCi2) are opened on either side to define the in-plane profile by the jaws only.

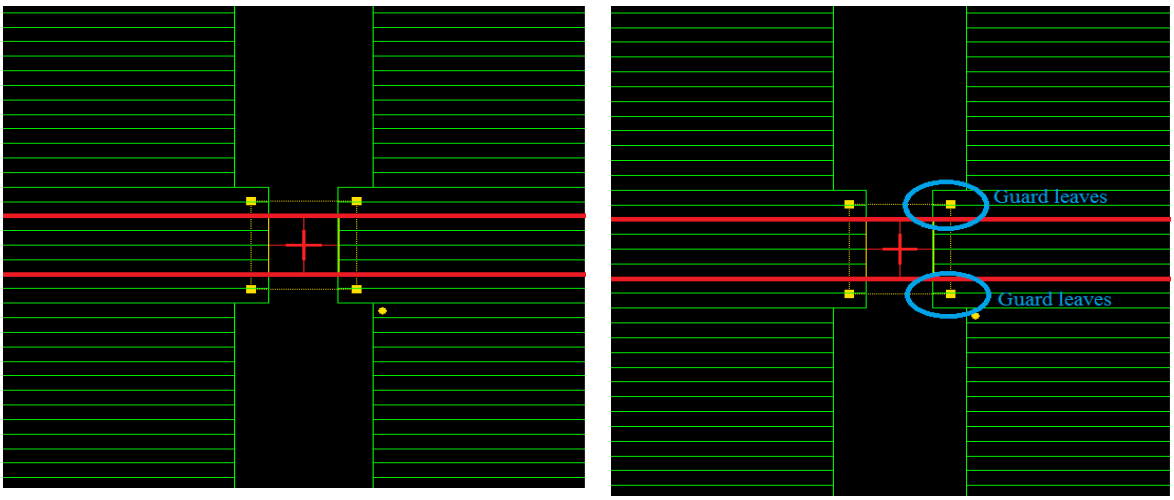

Appendix.2. Patient-specific quality control test for halcyon accelerator

Halcyon Accelerator (Eclipse TPS) Patient-specific quality control.

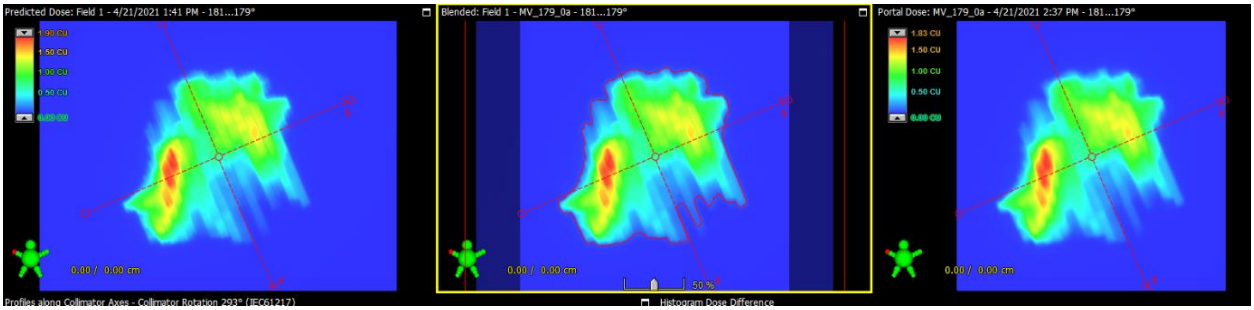

Fig.32. Halcyon accelerator fluence map for field 1

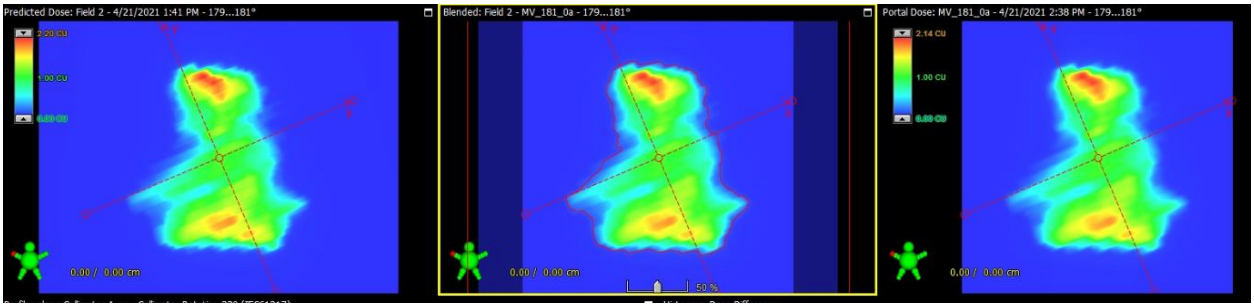

Fig. Halcyon accelerator fluence map for field 2.

Appendix.3. In-plane and cross profile profiles data

Table. In-Plane and cross-plane profiles

TPS calculated In-plane profile		**TPS calculated Cross-plane profile**	
Off-axis distance (cm)	Relative dose (%)	Off-axis distance (cm)	Relative dose (%)
-5	0.89	-5.0	1.15
-4.9	0.94	-4.9	1.08
-4.8	0.93	-4.8	1.22
-4.7	0.97	-4.7	1.09
-4.6	0.99	-4.6	1.04
-4.5	0.92	-4.5	1.14
-4.4	1.00	-4.4	1.31
-4.3	1.03	-4.3	1.22
-4.2	0.99	-4.2	1.26
-4.1	1.03	-4.1	1.20

-4.0	1.10	-4.0	1.28
-3.9	1.10	-3.9	1.23
-3.8	1.11	-3.8	1.25
-3.7	1.17	-3.7	1.34
-3.6	1.25	-3.6	1.28
-3.5	1.22	-3.5	1.42
-3.4	1.14	-3.4	1.48
-3.3	1.2	-3.3	1.52
-3.2	1.27	-3.2	1.54
-3.1	1.36	-3.1	1.52
-3	1.43	-3.0	1.6
-2.9	1.47	-2.9	1.63
-2.8	1.5	-2.8	1.71
-2.7	1.5	-2.7	1.8
-2.6	1.52	-2.6	1.83
-2.5	1.53	-2.5	1.97
-2.4	1.71	-2.4	2.13
-2.3	1.91	-2.3	2.19
-2.2	1.96	-2.2	2.48
-2.1	2.13	-2.1	2.85
-2	2.35	-2	3.14
-1.9	2.7	-1.9	3.72
-1.8	3.35	-1.8	4.61
-1.7	3.75	-1.7	5.85
-1.6	4.73	-1.6	7.64
-1.5	6.67	-1.5	10.2
-1.4	9.45	-1.4	14.75
-1.3	14.16	-1.3	21.78
-1.2	23.35	-1.2	32.59
-1.1	40.99	-1.1	46.24
-1	62.59	-1	63.36
-0.9	80.01	-0.9	75.51
-0.8	88.04	-0.8	87.11
-0.7	94.15	-0.7	91.84
-0.6	96.52	-0.6	95.8
-0.5	96.83	-0.5	97.68
-0.4	98.68	-0.4	97.73
-0.3	98.64	-0.3	99.72
-0.2	99.65	-0.2	98.19
-0.1	98.45	-0.1	99.29

0	100	0	100
0.1	99.94	0.1	101.49
0.2	98.9	0.2	99.41
0.3	99.16	0.3	99.23
0.4	99.06	0.4	99.21
0.5	98.18	0.5	98.41
0.6	96.32	0.6	93.82
0.7	94.13	0.7	91.58
0.8	88.95	0.8	86.57
0.9	77.77	0.9	75.94
1.0	63.29	1.0	62.91
1.1	40.32	1.1	47.64
1.2	23.19	1.2	33.11
1.3	14.53	1.3	21.67
1.4	9.21	1.4	14.91
1.5	6.40	1.5	10.56
1.6	4.70	1.6	7.72
1.7	3.90	1.7	5.71
1.8	3.34	1.8	4.73
1.9	2.76	1.9	3.84
2.0	2.52	2.0	3.18
2.1	2.26	2.1	2.68
2.2	2.13	2.2	2.33
2.3	1.91	2.3	2.14
2.4	1.77	2.4	2.14
2.5	1.82	2.5	2.04
2.6	1.71	2.6	2.03
2.7	1.58	2.7	1.66
2.8	1.54	2.8	1.61
2.9	1.34	2.9	1.59
3.0	1.36	3.0	1.56
3.1	1.52	3.1	1.49
3.2	1.30	3.2	1.53
3.3	1.30	3.3	1.49
3.4	1.25	3.4	1.53
3.5	1.22	3.5	1.37
3.6	1.21	3.6	1.34
3.7	1.20	3.7	1.42
3.8	1.12	3.8	1.38
3.9	1.11	3.9	1.23

4.0	1.01	4.0	1.28
4.1	1.06	4.1	1.26
4.2	1.08	4.2	1.20
4.3	1.01	4.3	1.19
4.4	1.00	4.4	1.16
4.5	0.92	4.5	1.19
4.6	0.93	4.6	1.15
4.7	0.92	4.7	1.10
4.8	0.98	4.8	1.22
4.9	0.90	4.9	1.06
5.0	0.88	5.0	1.12